Methane optical density measurements with an integrated path differential absorption lidar from an airborne platform

Haris Riris,[a*] Kenji Numata,[a] Stewart Wu,[a] Brayler Gonzalez,[a] Michael Rodriguez,[b] Stan Scott,[a] Stephan Kawa,[a] Jianping Mao[c]

[a] NASA Goddard Space Flight Center, 8800 Greenbelt Rd., Greenbelt, MD 20771,
[b] Sigma Space Corporation., 4600 Forbes Blvd., Lahnam, MD 20706,
[c] Earth System Science Interdisciplinary Center (ESSIC), University of Maryland, College Park, MD 20740

Abstract. We report on an airborne demonstration of atmospheric methane (CH_4) measurements with an Integrated Path Differential Absorption (IPDA) lidar using an optical parametric amplifier (OPA) and optical parametric oscillator (OPO) laser transmitter and sensitive avalanche photodiode detector. The lidar measures the atmospheric CH_4 absorption at multiple, discrete wavelengths near 1650.96 nm. The instrument was deployed in the fall of 2015, aboard NASA's DC-8 airborne laboratory along with an in-situ spectrometer and measured CH_4 over a wide range of surfaces and atmospheric conditions from altitudes of 2 km to 13 km. In this paper, we will show the results from our flights, compare the performance of the two laser transmitters, and identify areas of improvement for the lidar.

Keywords: lidar, spectroscopy, methane, optical parametric amplifiers, optical parametric oscillators, airborne instruments.

*E-mail: haris.riris@nasa.gov

1 Introduction

Methane (CH_4) is the second most important anthropogenic greenhouse gas (GHG) with a higher radiative forcing potential than Carbon Dioxide (CO_2) on a per molecule basis[1], making anthropogenic CH_4 a critical target for mitigation. The current CH_4 global mixing ratio is 1852 parts per billion (ppb)[2, 3]. Anthropogenic CH_4 is responsible for a significant portion of the global warming produced by all well-mixed greenhouse gases and contributes to the formation of ozone[4], another GHG and air pollutant.

Despite the critical importance of CH_4 for climate, the existing CH_4 observing network has proven inadequate to constrain global, regional, and sectoral sources, and explain observed trends and variation in atmospheric CH_4 over the last few decades. Therefore, there is a critical need for CH_4 observations for constraining the strength and distribution of methane's sources, including natural (e.g., wetlands) and anthropogenic (e.g., energy sector) ones. For instance,

35 much of the year-to-year variations in methane's global growth rate are likely from variations in

36 wetland emissions and part of the recent increasing trend in methane's growth rate may be

37 associated with increased energy extraction activities[5, 6]. An adequate CH_4 observing network is

38 necessary to monitor the interaction between the carbon cycle and climate change, such as the

39 potential release of CH_4 from stored carbon reservoirs (e.g., Arctic and boreal soils) and changes

40 in natural emissions. The current CH_4 observing network does not provide the necessary data to

41 understand and constrain methane's sources, such as from permafrost thaw, wetlands, which

42 challenges our ability to make confident projections of future climate. The importance of

43 measuring CH_4 is also reflected in the last National Research Council Decadal Survey for Earth

44 Science[7] and the recent report by the Carbon Climate Workshop[8].

45 Our current understanding of CH_4 distributions and processes is founded mostly on precise and

46 accurate ground-based, in-situ measurements from global monitoring networks[9, 10]. The location

47 and frequency of these measurements is, however, very sparse on a global scale and is even

48 sparser at high latitudes where the thawing Arctic permafrost is of particular concern. Large

49 quantities of organic carbon are stored in the Arctic permafrost and a warming climate can

50 induce drastic changes in carbon emissions and a subsequent positive feedback mechanism that

51 can significantly accelerate climate change[11].

52 Global measurements from satellites are available from passive optical sensors AIRS[12],

53 SCIAMACHY[13, 14], TES[15], IASI[16], and GOSAT[17], but currently lack the required sensitivity to

54 derive regional CH_4 sources. Passive sensors measuring reflected sunlight are limited to sunlit

55 areas of the planet and their sensitivity falls off at low sun angles, increasing cloud cover, aerosol

56 scattering, and low surface reflectivity. Recent observations indicate that the thawing Arctic

57 permafrost is active even during the cold season[18] highlighting the need for continuous sampling

58 at high latitudes even in the winter months.

59 The benefit of active sensing missions is that they provide global CH_4 measurements where they

60 are really needed: in the absence of sunlight (i.e., at night and at high latitudes in all seasons), in

61 the presence of scattered or optically thin clouds and aerosols, over land and water surfaces, and

62 with higher accuracy and precision than currently available. Active measurements using laser

63 remote sensing technology will be a key step in obtaining measurements of CH_4 from orbit with

64 sufficient coverage, sampling, accuracy and precision to address key science questions. The

65 French Centre National d'Etudes Spatiales (CNES) in collaboration with the German Aerospace

66 Centre (DLR) are developing an active methane mission called MERLIN (Methane Remote

67 Sensing Lidar Mission) scheduled for launch in 2021[19, 20]. The MERLIN mission targets an 8-36

68 ppbv relative random error in the methane column abundance with a 50 km horizontal resolution.

69 At NASA Goddard Space Flight Center (GSFC), we have been developing an active, airborne

70 lidar to measure atmospheric methane using Integrated Path Differential Absorption (IPDA) as a

71 precursor to a space mission to measure CH_4 from orbit.

72 **2   Instrument Description**

73 An IPDA lidar measures the absorption of laser pulses by a trace gas when tuned to a wavelength

74 coincident with an absorption line[21-31]. Using the instrument in a sounding (surface reflection)

75 mode which enables integrated column trace gas measurements from orbit with relatively modest

76 laser power.

77 The GSFC IPDA lidar uses a tunable, narrow-linewidth light source and a photon-sensitive

78 detector coincident with a CH_4 absorption at 1650.96 nm. The CH_4 spectrum at 1650.96 nm is

79 well suited for active remote sensing. The CH_4 line is mostly isolated from adjacent CO_2 lines

80   and there is very little water (H_2O) vapor interference. The MELRIN line at 1645.55 nm is less

81   suitable for our technique because it is interfered with by H_2O vapor at ~1645.47 nm and it is

82   wider than our line (~56 pm vs. ~36 pm), an important consideration because it increases the

83   tuning requirement for our laser transmitter. Fig. 1 shows the two-way atmospheric transmittance

84   spectrum around 1650.96 nm from a 400 km orbit using the 2008 HITRAN database[32] and a US
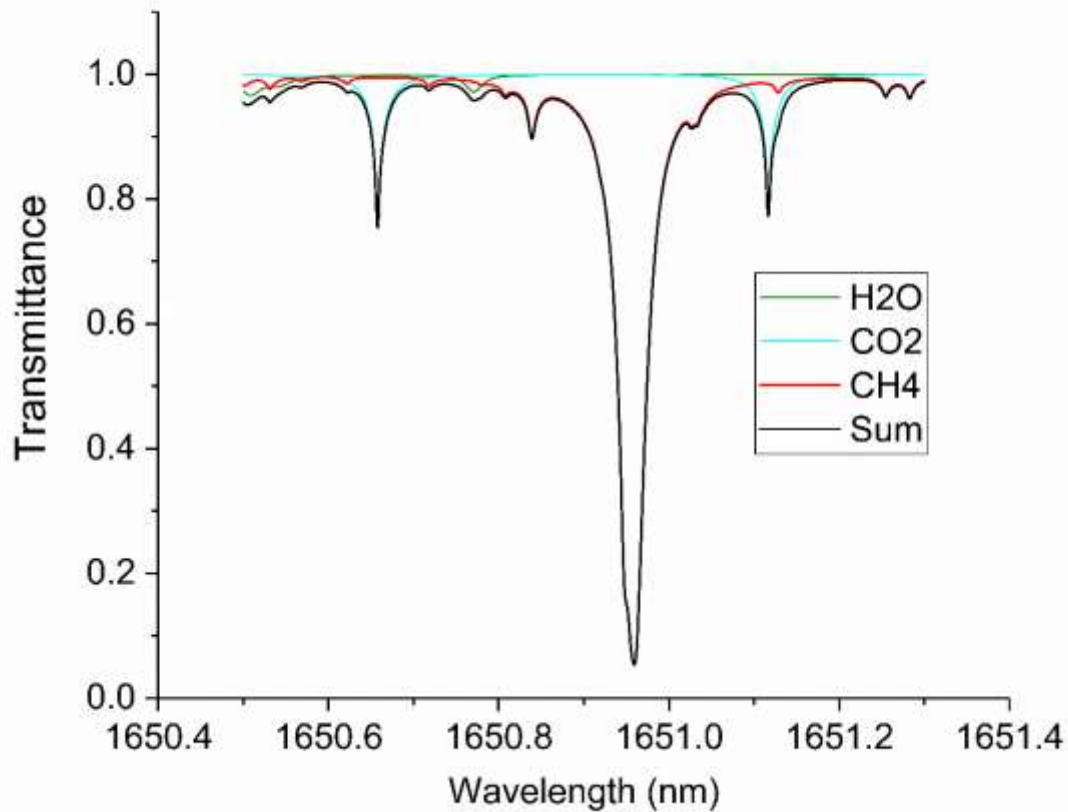
85   standard atmosphere.

86

87   **Fig. 1.** Two-way atmospheric transmittance near 1650.96 nm a from a 400 km orbit using the 2008 HITRAN
88   database and a US standard atmosphere. The CH_4 line is mostly isolated from adjacent CO_2 and H_2O vapor lines.
89

90   Although in principle, only two wavelengths ("on" and "off" the line) are needed to determine

91   the transmittance through the atmospheric column, our technique uses multiple wavelengths to

92 probe the absorption feature. Using multiple wavelengths can reduce errors that may affect the

93 measurement precision[33], measure the spectral shift of the line with changing atmospheric

94 pressure[34], generate atmospheric backscatter profiles of the entire column[35], and enable retrievals

95 of trace gas mixing ratios above and below the planetary boundary layer[36].

96 An early version of our instrument[25] flew in 2011. The major differences between the system in

97 ref. 25 and the new instrument are: 1) the detector: in 2011 we used a very low (<1%) quantum

98 efficiency (QE) photomultiplier tube (PMT) with very limited dynamic range. The new

99 instrument used an enhanced avalanche photodiode (e-ADP) with ~90% QE. 2) The type and

100 energy of the transmitter(s): In 2011, we used a low energy Optical Parametric Amplifier (OPA)

101 laser transmitter with pulse energy of ~10 μJ. The new airborne lidar used an OPA and an

102 Optical Parametric Oscillator (OPO) with pulse energies of ~25 μJ and ~250 μJ respectively. 3)

103 The opto-mechanical layout and data acquisition system were completely redesigned and

104 considerably improved. As a result, spurious effects such as etalon fringes were dramatically

105 reduced which improved the precision of the instrument.

106 Our new airborne IPDA lidar used two different laser transmitters. The first is an Optical

107 Parametric Amplifier (OPA) and the second is an Optical Parametric Oscillator (OPO). Only one

108 laser transmitter is used at a time by using a movable mirror to select the desired transmitter. A

109 simplified block diagram of our lidar is shown in Fig. 2 and is based on our previous work with

110 optical parametric generation[37].

111 The OPA, used 20 wavelengths, but was simpler to implement than the OPO, because it did not

112 require an optical resonator cavity, was easier to align and tune, and used only two seed lasers.

113 However, it is extremely difficult to scale the OPA energy to the level needed for space and still

114 maintain a narrow linewidth. Depending on the receiver size and other instrument parameters

115   we calculate that approximately 600 µJ is needed to obtain a measurement with a 0.5% precision.

116   The underlying reason for the wider linewidth is the large mismatch between the seed and pump

117   energies, which makes it very difficult to amplify the seed with the desired spectral

118   characteristics.   If the seed laser power can be significantly scaled up and back-conversion can

119   be suppressed then it may be possible to achieve energies of 600 µJ out of the OPA with the

120   desired spectral characteristics.

121   In the OPO, narrow linewdith is achieved by using an optical resonator cavity, which also

122   enhances the energy of the non-linear conversion. Our OPO uses five wavelengths and a 1.2 mJ

123   GSFC-built solid-state pump laser with a triangular optical ring cavity. The OPO energy could

124   be scaled to space (~600 µJ) and maintain a narrow linewidth with a suitable higher energy pump

125   laser and improved optical design. However, the OPO currently requires a separate seed laser

126   and complex optical phase-lock loops for each wavelength used.

Fig. 2. Simplified functional block diagram of our IPDA lidar. The lidar can use one of two different laser transmitters using a movable selection mirror: An Optical Parametric Amplifier (OPA) or an Optical Parametric

7

130 Oscillator (OPO). The transmitters use DFB diode lasers for seed lasers but different pump lasers. Only one laser
131 transmitter is operating during flight.
132

133 The first transmitter option (OPA) consists of a magnesium oxide-doped periodically poled

134 Lithium Niobate (MgO:PPLN) crystal which is pumped by a pulsed single-frequency 1064 nm

135 laser and seeded by a continuous-wave (CW) 1650.96 nm laser diode. The pump laser is a

136 custom burst-mode Yb fiber laser from Fibertek Inc., based on a Master Oscillator Power

137 Amplifier (MOPA) configuration[38]. The pump laser was optimized for high peak power and

138 generated 600 µJ in a burst pulse. Each burst pulse consists of twenty individual 3 ns pulses

139 separated by 85 ns with the individual pulse energies in the burst varying from 2 to 10 µJ. An
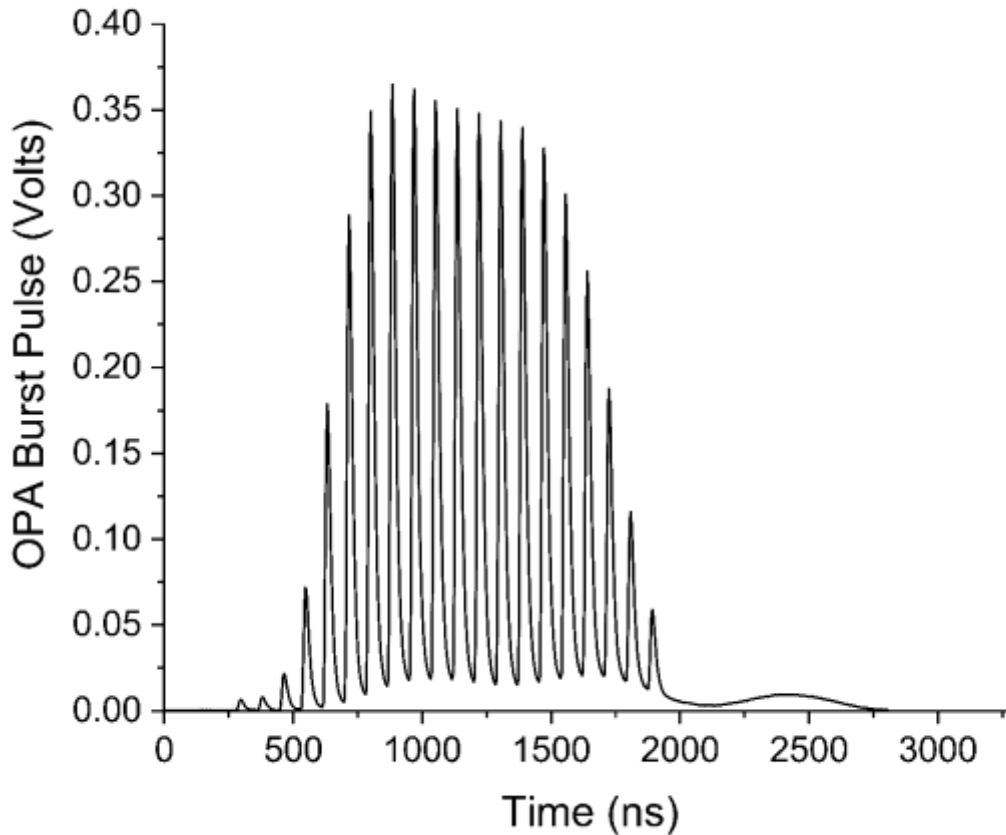
140 example of the OPA burst pulse is shown in Fig. 3.

Fig. 3. Example of temporal shape of the OPA burst pulse from the energy monitor detector showing individual pulses within the burst pulse.

The OPA output varies non-linearly with the peak power of the pump so the variation in the individual pump pulses resulted in very low conversion in the OPA of the low energy pulses. The linewidth of the OPA was ~500 MHz. The pump laser was delivered with a bare, large mode area (LMA) fiber output that optimized the power output but was not suitable for flight. Prior to our flights, we connectorized the output and the burst pulse energy was reduced to 350 µJ per burst pulse.

Two distributed-feedback (DFB) CW diode lasers, a master reference and a scanning seed, from NEL America (NLK1U5FAAA), are used in the OPA. The wavelength of the master reference

153 laser is locked on the absorption peak at ~ 1650.96 nm using a 16.5 cm cell containing ~40 mbar

154 of CH_4. The locking technique is the same for both the OPA and OPO, and is described by

155 Numata[39, 40]. It is based on the technique used by Pound–Drever–Hall[41] and is similar to the

156 technique used by Fix[42]. We estimate that the long-term drift of the master laser frequency is ~

157 2 MHz, based on our experience with similar DFB seed lasers for CO_2.

158 The scanning seed laser is tuned over the CH_4 line by rapidly scanning the laser current. The

159 beat signal between the master reference laser and the scanning seed laser is measured by a

160 frequency counter and recorded by the data acquisition system. The frequency of the beat signal

161 is converted into the OPA wavelengths in post-processing.

162 The scanning seed and pump laser beams are combined with a beam combiner and focused

163 through the PPLN crystal. The temperature of the PPLN crystal can be temperature-tuned to

164 optimize the phase matching at the seed wavelength. The unconverted pump beam at 1064 nm is

165 separated from the signal beam at 1650.96 nm using a dichroic mirror and directed into a beam

166 dump. A small part of the OPA beam at 1650.96 nm is also directed through an 8 cm reference

167 cell containing ~170 mbar of CH_4 for calibration purposes and a blocking filter prevents any

168 remaining 1064 nm radiation from existing the aircraft. The main OPA output beam is directed

169 through a beam expander to reduce its divergence. The final output energy of the OPA

170 transmitter exiting the aircraft was approximately 25 µJ per burst pulse and 20 wavelengths were

171 used in each wavelength scan to sample the CH_4 lineshape.

172 The second transmitter (OPO) consists of another temperature controlled PPLN crystal inside a

173 three-mirror cavity. The temperature of the PPLN crystal can be temperature-tuned to optimize

174 the phase matching at the seed wavelength. The OPO is pumped by a pulsed single-frequency

175 1064 nm Nd:YAG laser and seeded by five CW DFB lasers at ~1650.96 nm.

176   The pump laser of the OPO is a custom-made GSFC single frequency Nd:YAG laser with a ~60

177   ns pulse width and maximum energy of 1.2 mJ per pulse at a 5 kHz repetition rate.

178   The same master reference seed laser used in the OPA is used for the OPO. Part of the phase-

179   modulated master reference beam (labelled "locking beam" in Fig. 2) is used to lock the OPO

180   cavity using a cavity length-control servo and a piezo electric transducer (PZT). Four additional

181   slave DFB diode lasers are offset-locked to the master reference laser by an integral number of

182   the OPO cavity free-spectral range (FSR) using the beat signal from four detectors and four

183   optical phase locked loop servos and a Rubidium frequency reference. Thus, the OPO samples

184   the CH_4 absorption at five wavelengths (one master and four slave). The wavelengths are

185   selected by switching fast (NanoSpeed™) 1x2 fiber optic switches made by Agiltron.

186   After exiting the OPO cavity the unconverted pump beam at 1064 nm is separated from the

187   signal beam at 1650.96 nm using a dichroic mirror and directed into a beam dump. After the

188   dichroic mirror, a small part of the OPA beam at 1650.96 nm is directed through a 5 cm CH_4

189   reference cell containing ~260 mbar of CH_4 for calibration purposes and a blocking filter

190   prevents any remaining 1064 nm radiation from existing the aircraft. The main OPO output

191   beam is directed through a beam expander to reduce its divergence. The maximum output energy

192   of the OPA transmitter exiting the aircraft was approximately 250 μJ per pulse. The measured

193   linewidth of the OPO was less than 300 MHz but the measurement was limited by the resolution

194   of the Febry-Perot etalon we used[39].

195   The divergence for both laser transmitters was ~150 μrad. Prior to exiting the aircraft through

196   the nadir port, a wedged beam splitter sends a small portion of the outgoing beams (~4 %) to an

197   8.9 cm diameter integrating sphere with two InGaAs detectors attached to one of its ports (one

198   for the OPA and one for the OPO). The detectors measure the outgoing energy monitor pulses

199   for the OPO or OPA and are digitized by the data acquisition system. The energy monitor pulses

200   are used to normalize the reflected pulses from the ground every 1/16 second in post processing.

201   In addition to the energy monitors, a multimode 200-μm core fiber is also connected to a port of

202   the integrating sphere and collects a small fraction of the outgoing laser energy. The multimode

203   fiber output is collimated and fed back into the receiver telescope and on focused on our

204   sensitive detector to provide a zero range pulse (or "start pulse") for our ranging algorithm. The

205   time of flight from the zero range pulse to the reflected pulses from the ground is used to

206   determine the IPDA lidar range.

207   The laser pulses reflected from the ground are collected by a commercial 20 cm diameter

208   receiver telescope (Vixen VC200L) with an effective focal length of 2 m and are coupled into an

209   anti-reflection (AR) coated 600-μm core multi-mode fiber. The receiver field of view (FOV)

210   was 300 μrad. The receiver fiber output is collimated by a lens and directed through a 0.8 nm

211   (FWHM) band pass filter, and then focused onto a HgCdTe enhanced avalanche photodiode (e-

212   ADP) by DRS Technologies[43-45]. The detector is a 4x4-pixel array, with the pixel pitch being 80

213   μm with no gaps between pixels. The detector is operated at 80K and its electrical bandwidth is

214   ~7 MHz.

215   The signals from the frequency counter, reference cell (OPA or OPO), the energy monitor (OPA

216   or OPO), the zero range pulse, and ground return pulses are digitized by a National Instruments[©]

217   PXI-based data acquisition system containing a FlexRIO FPGA Module, a FlexRIO Digitizer

218   Adapter Module, a Timing and Synchronization Module, and a Global Positioning System (GPS)

219   module. All signals are averaged every 1/16 second and the files are time stamped by the GPS

220   time. Additional averaging can be performed in post-processing. The major parameters of the

221   airborne IPDA lidar are summarized in Table 1 below.

222   **Table 1 Instrument Parameters**

Parameter	OPA	OPO
Center Wavelength	1650.958 nm	1650.958 nm
Number of wavelengths used	20	5
Transmitter Energy/pulse	~25-30 μJ	~250 μJ
Transmitter Pulse rate	10 kHz	5 kHz
Transmitter divergence	~150 μrad	~150 μrad
Spectral Linewidth	~500 MHz	<300 MHz[*]
Number of seed lasers used	2	5
Pump laser	Burst mode Yb Fiber	Single pulse Nd:YAG
Pump laser energy	350 μJ	1.2 mJ
Receiver diameter	20 cm	20 cm
Receiver Field of view	300 μrad	300 μrad
Receiver band pass	0.8 nm (FWHM)	0.8 nm (FWHM)
Detector	4x4 HgCdTe e-ADP	4x4 HgCdTe e-ADP
Detector Pixel Pitch	80 μm	80 μm
Detector QE	~ 90%	~ 90%
Detector Temperature	80K	80K
Detector bandwidth	7 MHz	7 MHz
Averaging time	1/16 sec	1/16 sec

223   [*]Linewidth measurement limited by the resolution of the scanning Febry-Perot etalon used.

3   Airborne Demonstration Results

3.1 Flights

In late September 2015, the instrument was installed on the NASA DC-8 airborne laboratory,

based at Armstrong Flight Research Center Science Aircraft Integration Facility (SAIF) in

Palmdale, CA. The transceiver structure supported two small, vibration isolation, optical

benches for the OPO and OPA, the receiver telescope, and the transmit optics components. A

vibration isolation mechanism for the entire structure minimized the impact of aircraft vibrations.

The overall transceiver dimensions were approximately $0.9 \times 2.0 \times 0.8$ m^3 and the total weight was

363 kg (Fig. 4). Two aircraft racks on either side of the transceiver structure held ancillary

instrumentation needed for the operation of the instrument (data acquisition and control

computers, detector, seed lasers, electronics, chillers for the pump lasers, etc.).

235

Fig. 4. The GSFC IPDA lidar installed on the NASA DC-8 airborne laboratory, in Palmdale, CA. The transceiver structure supported two optical benches for the OPO and OPA, the receiver telescope, and the transmit optics components. The overall transceiver dimensions were approximately $0.9{\times}2.0{\times}0.8$ m^3 and the total weight was 363 kg. Two instruments racks on either side of the transceiver contained the control and data acquisition electronics.

A Picarro in-situ analyzer (Picarro G1301-m) measuring methane, carbon dioxide, and water vapor using Wavelength-Scanned Cavity Ring Down Spectroscopy was also installed at a different location in the aircraft to provide in-situ CH_4 reference measurements.

Three flights in the western United States were carried out in late September-early October 2015. Flight planning was constrained by the limited number of flight hours available, the inclement weather and aircraft maintenance issues. Each flight lasted about 4 hours and included several segments at increasing altitudes from 2 to 13 km over varying topography, ground reflectivity (including ocean), and atmospheric conditions. In addition, a spiral descent from ~13 km to near the surface (~30-300 m depending on Federal Aviation Administration flight clearances) was

250   included in the flight plan in order to sample the localized vertical profile of the CH_4 mixing

251   ratio and associated meteorological parameters (pressure, temperature, humidity, etc.) using the

252   Picarro in-situ sensor and the aircraft's data acquisition system. The IPDA lidar was always

253   turned off below 1 km above ground level (AGL) to comply with strict laser safety requirements.

254   Fig. 5 summarizes our flight paths in the western US. The flight tracks and locations were

255   chosen to minimize the transit flight time and targeted areas of potential CH_4 emission sources.
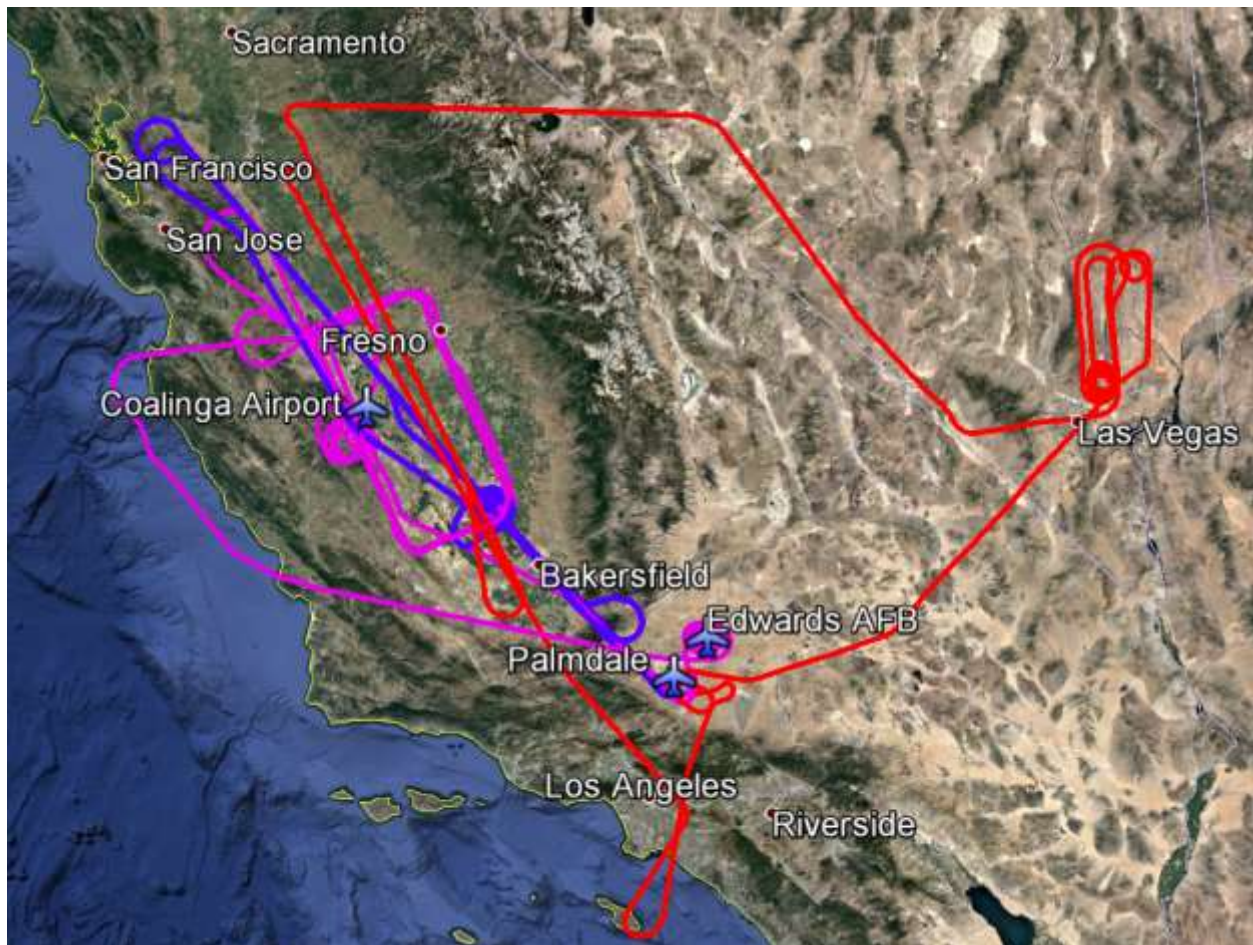

256
257   **Fig. 5** Fight tracks for the 2015 flights. Flight 1 (blue), Flight 2 (red), Flight 3 (magenta).
258

259   For the first two flights, we used the OPA transmitter and for the third flight, we used the OPO.

260   The first flight was mostly over the Central (San Joaquin) Valley of California. We flew on a

261   general south-north track, at three different altitudes at approximately 3.1, 5.9-6.0 km and 12.7

15

262 km. A large portion of the flight was in and over a dense cloud cover and the spiral descent

263 originally scheduled over Coalinga airport, CA was moved to approximately 40 km north of

264 Bakersfield, CA due to the weather conditions. The Coalinga airport was originally chosen due

265 to its proximity to a large feedlot.

266 The second flight targeted a large landfill approximately 30 km northeast of Las Vegas, NV.

267 After an initial pass at ~10 km and a subsequent spiral descent and low pass over the landfill at

268 ~300 m above ground level (AGL), two more flight segments were flown at 3.2 and 6.4 km.

269 Then we transited over to the Central Valley, CA where we did two high altitude north-south

270 flight segments at 12.7 and 13.1 km. Part of the Central Valley was completely covered by a

271 dense cloud cover during our flight.

272 The third flight was again over the Central Valley of California mostly due to adverse weather

273 conditions and flight restrictions at other candidate sites. We flew on a ~75×160 km^2 rectangular

274 path centered on the Central Valley at three different altitudes: 3.1, 6.3 and 12.7 km. A spiral

275 descent and low pass (~30 m AGL) was performed over Coalinga airport. Following the high

276 altitude segment at 12.7 km, we flew over the Pacific Ocean and performed another spiral

277 descent over Edwards Air Force Base (AFB), CA prior to landing in Palmdale.

278 The flight altitude profiles (GPS altitude and IPDA lidar range vs. time) are shown in Fig. 6.
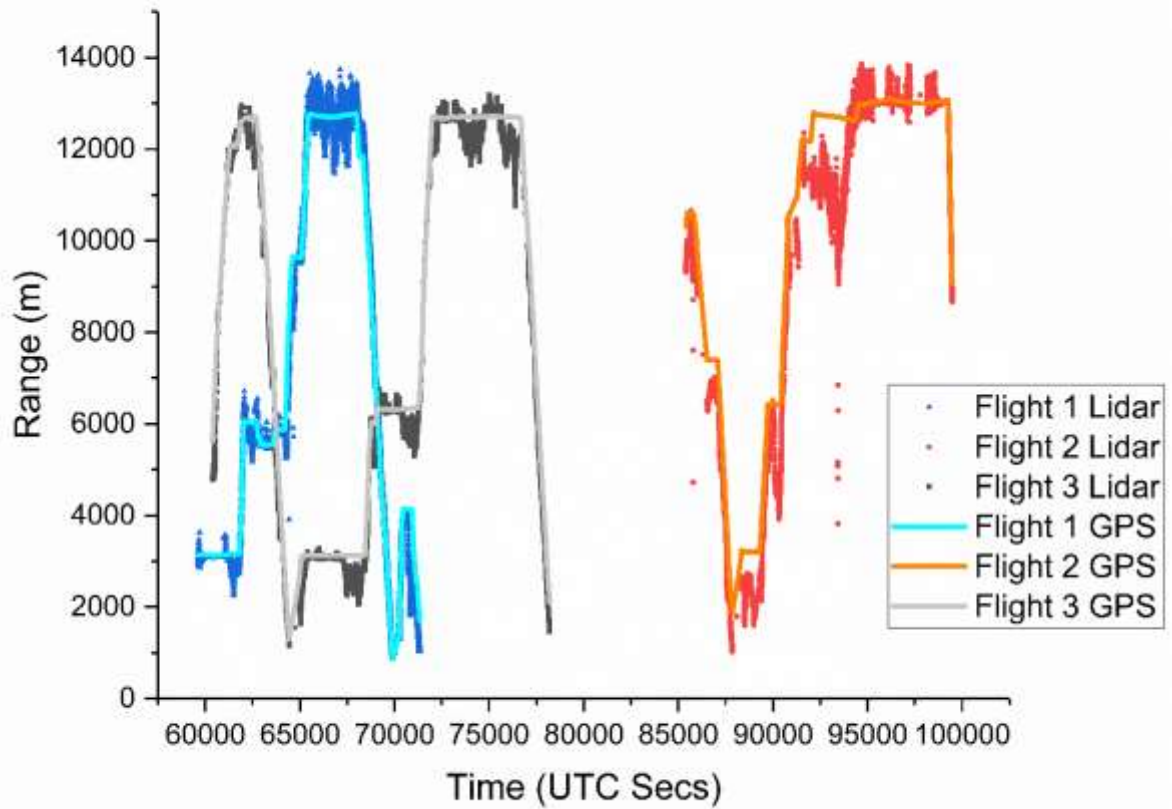
Fig. 6. Flight altitude (range) in m vs. time in UTC seconds since midnight as measured by the GPS receiver and our IPDA lidar for all three flights. The differences between the GPS and the IPDA lidar range are due to topography. The GPS measures the altitude above the mean sea level (or reference ellipsoid) but the IPDA lidar range is the altitude (range) above ground, which includes the topography.

3.2 Retrievals

Our retrieval algorithm uses a least squares fit to minimize the root mean squared error between

the IPDA lidar measurements and the model prediction and is similar to the approach used by

Abshire et.al.[46] in their CO_2 retrievals. The averaging time for the data acquisition system is

1/16 sec but the data is further averaged in post processing in 1-sec intervals. First, the range

(path length) from the aircraft to the surface is determined from the laser pulse time of flight

(TOF) by correlating the first return pulse with the zero range pulse and measuring the time

delay of the correlation peak, following the cross-correlation approach by Amediek[47]. The

292   aircraft is equipped with a GPS antenna and a radar altimeter and we compare our lidar range

293   with the radar range to ensure that that only valid ground return pulses are used in the retrievals.

294   If only cloud returns are present, the data is not used in the analysis. However, there were many

295   occasions we had multiple returns from cumulus and cirrus clouds, and the ground. Segments

296   that did not contain enough valid ground returns due to the presence of clouds or other

297   instrument issues were excluded from the analysis. Generally when fewer than 50% ground

298   returns are present over a 1-second averaging period the data were not used. The algorithm then

299   estimates the column average of CH_4 transmittance of the atmospheric column by fitting the

300   integrated pulse returns from the surface at each wavelength, after normalization by the

301   transmitted pulse energy, the filter transmission, and other instrument calibrations. The

302   algorithm compares the experimental with the theoretically calculated transmittance values and

303   adjusts the fit parameters, including the mixing ratio, to minimize the fit error. The theoretical

304   calculations used a Voigt lineshape, the lineshape parameters from the HITRAN 2008 database

305   and line-by-line radiative transfer calculations[48]. The impact of more complicated lineshape

306   functions and line mixing was not included in the calculations. However, recent spectroscopic

307   measurements by Delahaye[49] for the MERLIN line at 1645.55 nm suggest that differences of

308   1.5% up to 5% in the lineshape may arise if these effects are not taken into account. Fig. 7

309   shows a theoretical CH_4 lineshape from a 400 km altitude orbit with a US standard atmosphere,

310   and a comparison of the corresponding wavelength sampling by the OPA and OPO (20 vs. 5
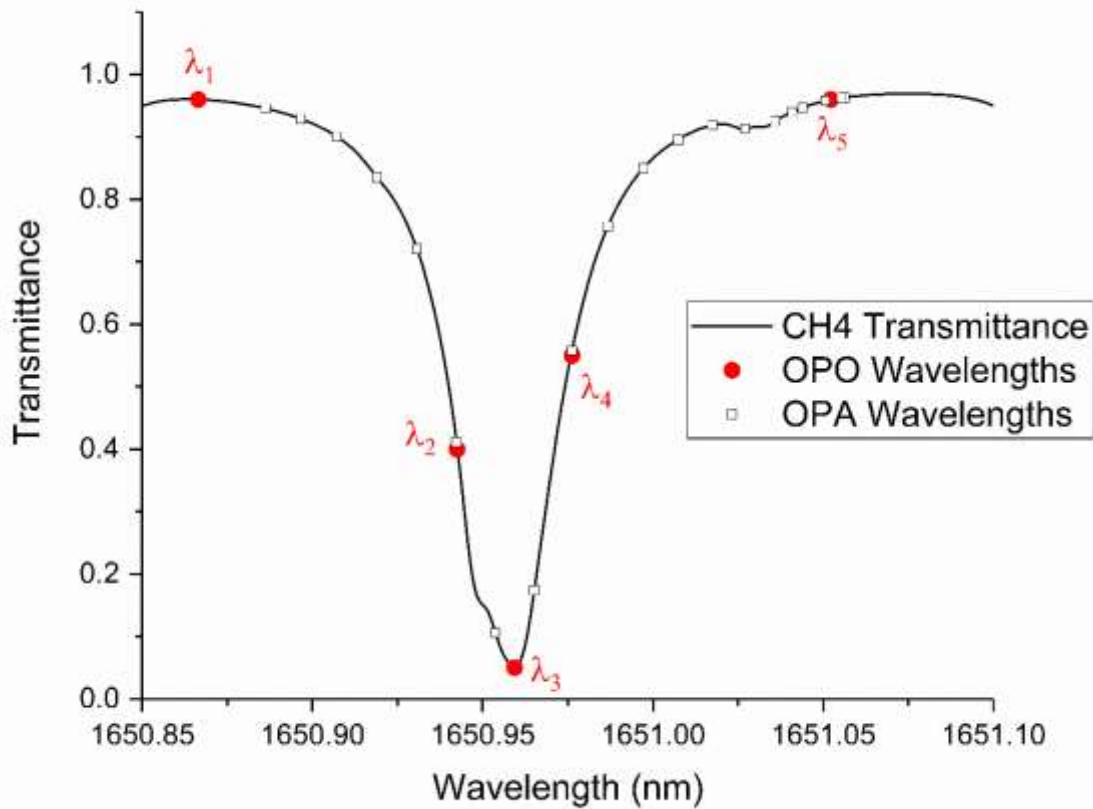
311   wavelengths).

317   The meteorological data for the vertical profile of the atmosphere are obtained from the spiral

318   descents, the Goddard Modeling and Assimilation Office (GMAO) Modern Era Retrospective -

319   Analysis for Research and Applications (MERRA) [50] and the Goddard Earth Observing System

320   Model, Version 5 (GEOS-5)[51] with a sampling-interpolating interval of 1 second. The true CH_4

321   mixing ratio profile over the entire flight path is of course, unknown. For simplicity, in our

322   analysis the CH_4 mixing ratio used in the radiative transfer calculations was set at a constant

323   1900 ppb. Although this value is clearly not an accurate estimate of the true mixing ratio for an

324   entire flight, it is not very different from the column average values obtained by the in-situ

325   spectrometer during our spirals and it provided a reasonable basis for estimating the precision,

326   but not necessarily the accuracy, of the IPDA lidar. In order to better assess the accuracy of an

327   IPDA lidar more frequent spirals and/or data from radiosondes are needed to infer the mixing

328   ratio profile over a flight path.

329   Fig. 8 shows the time series data of the in-situ CH_4 mixing ratio measured by the Picarro, the

330   theoretical CH_4 mixing ratio, set at 1900 ppb, and the CH_4 mixing ratio values obtained from our

331   retrieval algorithm for flight 1. There are obvious difference between the instrument retrievals

332   and those from the Picarro. That is to be expected since the Picarro is an in-situ measurement

333   and the lidar measures the column average.
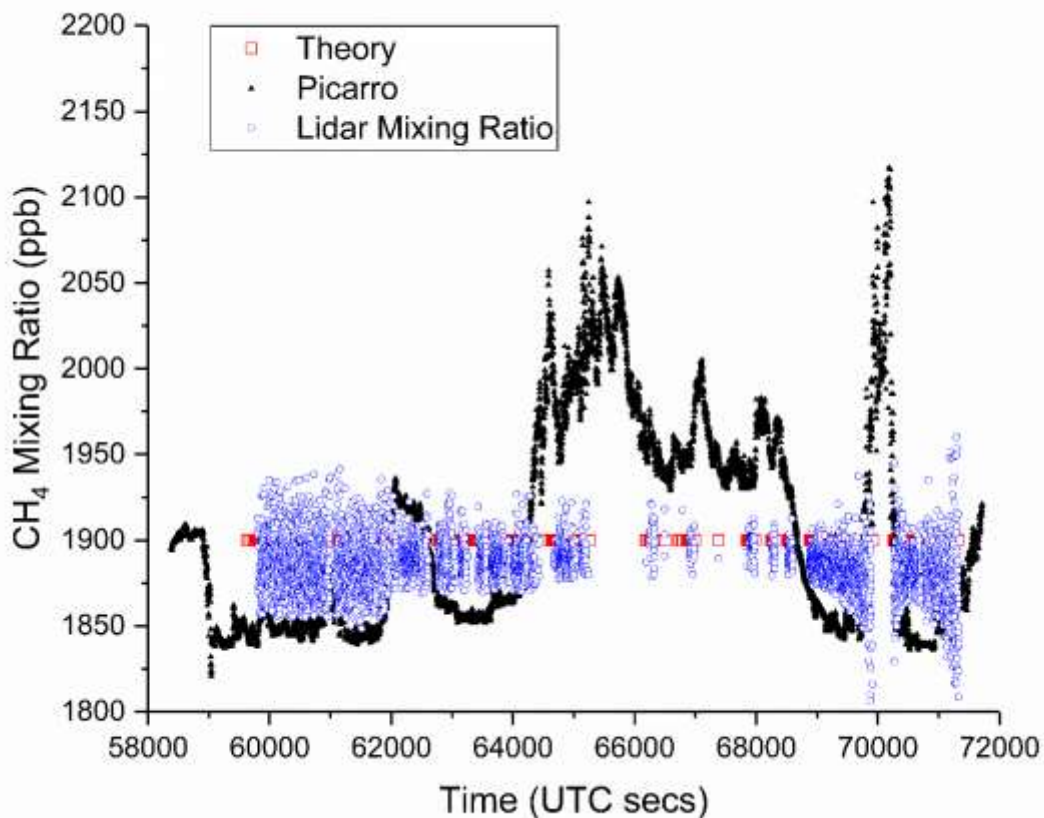

334
335   **Fig. 8.** Time series data for flight 1 showing the in-situ CH_4 mixing ratio as measured by the Picarro, the theoretical
336   CH_4 mixing ratio (set at 1900 ppbv), and the CH_4 mixing ratio values by our retrieval algorithm. Outliers due to
337   instrument adjustments and clouds were filtered out.
338

20

339 There were multiple outliers in our retrievals that were filtered out. These were mainly due to

340 two factors: instrument adjustments and optically thick clouds. Due to aircraft vibrations and

341 changes in the cabin temperature and pressure, the OPA transmitter needed alignment

342 adjustments during flight to re-optimize its power. In addition, the wavelength locking circuitry

343 and instrumentation that locked and reported the wavelength of each laser pulse, by measuring

344 the frequency of the beat note between the reference laser and the scanning seed laser

345 wavelengths, would occasionally report erroneous values. The average wavelength values are

346 used if the reported wavelength value did not deviate more than ± 20 pm from the moving

347 average wavelength value. Finally, a significant part of the flight was over broken, optically

348 thick clouds. When all the outliers due to broken clouds and instrument adjustments were

349 filtered out, the agreement between the theoretical CH_4 mixing ratio, set at 1900 ppb, and the

350 retrieved CH_4 mixing ratio values was very good and the standard deviation of the retrieved CH_4

351 mixing ratio was 14.9 ppb or ~0.8% (14.9 ppb/1900 ppb). Assuming the column average CH_4

352 mixing ratio did not vary significantly this value represents a reasonable estimate of the

353 measurement precision of our IPDA lidar. Another good way to assess the IPDA lidar

354 performance is to plot the experimentally retrieved differential optical depth (DOD) vs. the

355 theoretical value. The theoretical and experimental DOD values are determined by the

356 difference in optical depth (OD) between the on wavelength interpolated at the wavelength

357 closest to the peak (~1650.965 nm) and the average value of the OD at the off wavelengths to the

358 left and right of the absorption (~1650.887 and ~1651.056 nm respectively). After removing all

359 the outliers due to laser power adjustments, erroneous wavelength values and broken clouds, the

360 DOD Lidar vs. DOD Theory linear fit (Fig. 9) had a slope of 0.98 and an offset of -0.007. The
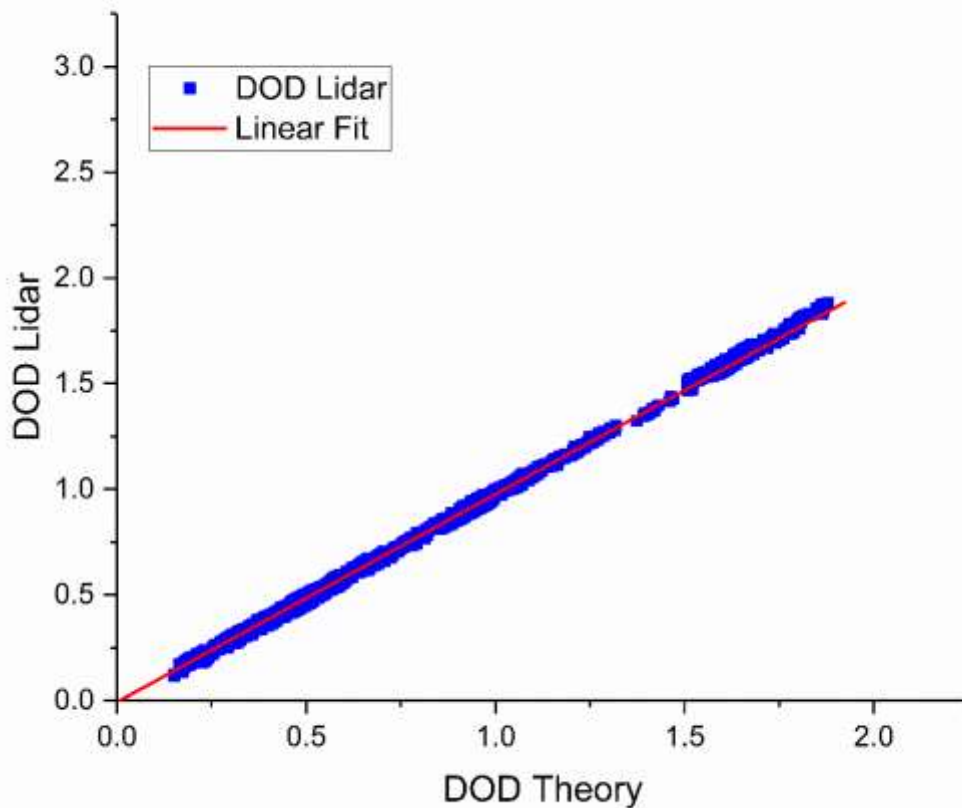
361 R^2 value was 0.994.

362
363   **Fig. 9.** Lidar DOD vs. Theoretical DOD for flight 1. The linear fit (without the outliers) had a slope of 0.98 and an
364   offset of -0.007 and R^2 value was 0.994.
365
366
367   **Fig. 10** Time series for flight 2 data showing the in-situ CH_4 mixing ratio as measured by the Picarro, the theoretical
368   CH_4 mixing ratio (set at 1900 ppbv), and the CH_4 mixing ratio values by our retrieval algorithm. Outliers due to
369   instrument adjustments and clouds were filtered out.
370   . The standard deviation of the retrieved CH_4 mixing ratio was 13.4 ppb or ~0.7% (13.4

371   ppb/1900 ppb). The DOD Lidar vs. DOD Theory linear fit for flight 2 had a slope of 0.998 and

372   an offset of -0.007 (Fig. 11. Lidar DOD vs. Theoretical DOD for flight 2. The linear fit (without

373   the outliers) had a slope of 0.998 and an offset of -0.007 and R^2 value was 0.990. The R^2 value

374   was 0.990. These values are consistent with flight 1 results indicating that when the instrument

375   is operating properly (i.e. no adjustments are being made and no cloud interferences) it is capable

376   of measuring CH_4 mixing ratios with a 0.7-0.8 % precision. Obviously, the definition of the

22

377   instrument "operating properly" is subjective and in our case, it excluded sections of the flights

378   where the instrument needed adjustments. However, the current results provide "proof-of-

379   principle" evidence that a multi-wavelength IPDA lidar with an OPA can provide high enough

380   precision for meaningful science measurements from an airborne platform over a varying

381   topography and altitudes from 2 to 13 km.
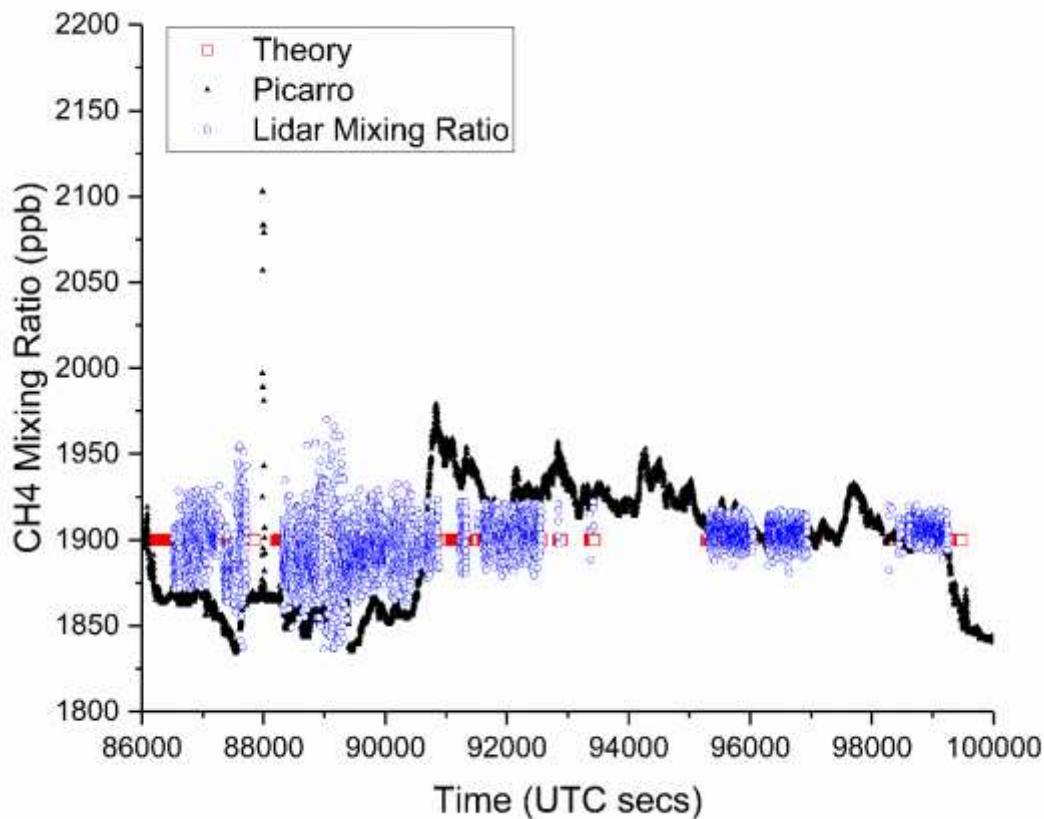

382
383   **Fig. 10** Time series for flight 2 data showing the in-situ CH_4 mixing ratio as measured by the Picarro, the theoretical
384   CH_4 mixing ratio (set at 1900 ppbv), and the CH_4 mixing ratio values by our retrieval algorithm. Outliers due to
385   instrument adjustments and clouds were filtered out.

386   .

387
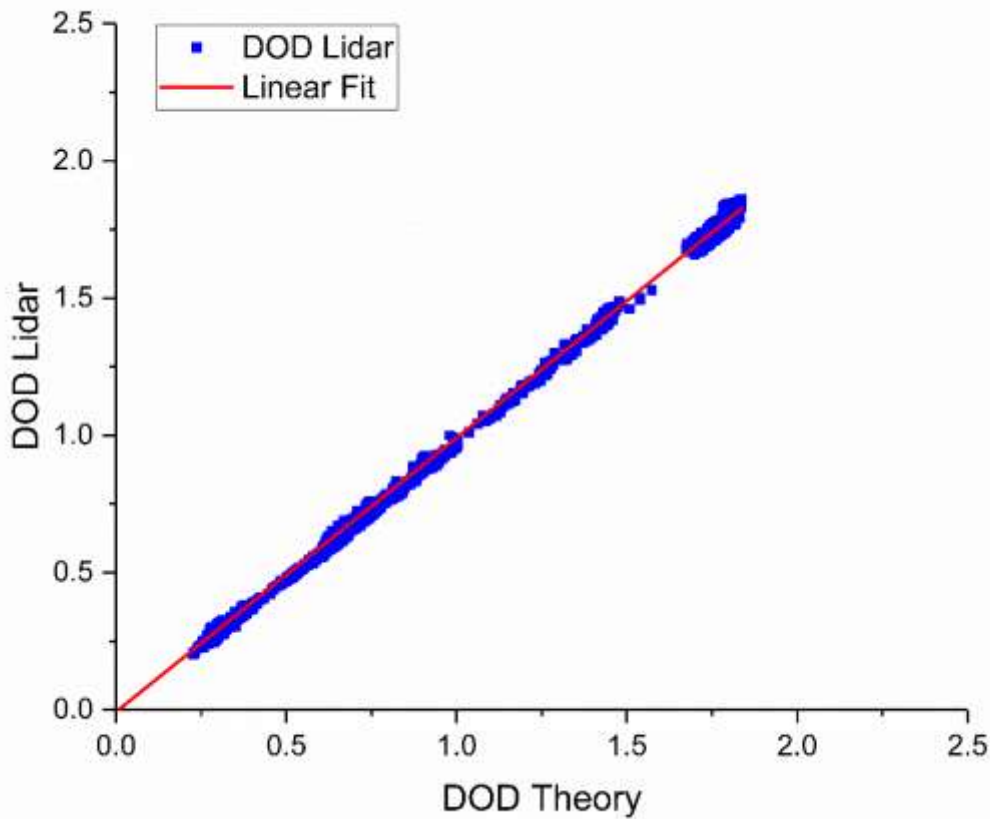388   **Fig. 11.** Lidar DOD vs. Theoretical DOD for flight 2. The linear fit (without the outliers) had a slope of 0.998 and an
389   offset of -0.007 and R^2 value was 0.990.
390

391   The last flight (flight 3) used the OPO as the laser transmitter. As shown in Table 1, the OPO

392   used only five wavelengths vs. twenty for the OPA. Fewer wavelengths means that the lineshape

393   is under-sampled and thus, it is more difficult to identify and remove any baseline slope and/or

394   other artifacts in the data. The OPO transmitter also required adjustments during flight. In

395   addition, the high OPO energy (~250 µJ) presented additional challenges. It saturated our

396   detector especially at lower altitudes. Our initial plan to attenuate the received energy by

397   restricting the receiver aperture size with a variable iris did not work for the flight configuration

398   on the DC-8, even though we tested the idea successfully in the laboratory. The hardware that

399   was used to restrict the receiver aperture size produced a large near field backscatter when

400   installed in the aircraft saturating and turning off the DRS detector. As a result, it could not be

401   used for flight and thus, the OPO energy was too high for the detector, especially for the low

402   altitude flight segment and over highly reflective surfaces. The detector gain had to be turned

403   down to its minimum value for part of the flight where the detector was presumed to be non-

404   linear. Our initial analysis showed a large discrepancy between the theoretical and experimental

405   DOD values. More importantly, we expected the discrepancy to be worse for the lower altitude

406   segment of the flight, where the detector was saturated and the gain was turned down to a

407   minimum. Contrary to our initial expectations, the DOD discrepancy was worse for the higher

408   altitude segment of the flight, where the detector was not saturated and operating in a linear

409   regime. Repeated post-flight calibrations of the DRS detector in the laboratory failed to uncover

410   any significant detector non-linearities within the digitizer dynamic range (1.23 V peak-peak)

411   that could account for the discrepancy we observed. For a given detector gain (bias) above

412   threshold, the detector is linear over at least two orders of magnitude and even when the detector

413   gain is set to its minimum value the results were repeatable and could be calibrated. Another

414   possible problem we uncovered in our post flight calibration was wavelength locking.

415   Wavelength 1 (λ_1) was initially reporting a "lock" status even though it was not always properly

416   locked on the correct wavelength. The problem was corrected quickly during flight (shortly after

417   the first spiral around 64000 secs UTC) but the data prior to the correction had to be discarded.

418   We hypothesized that the other wavelengths might have also experienced the same issue later in

419   the flight. Several post-flight calibrations in the laboratory with a high-resolution wavemeter

420   showed that the wavelength locking circuitry was operating properly and the circuitry was

421   reporting the wavelength values correctly. A detailed analysis of the OPO reference cell

422   indicated that the discrepancy was not due to the detector or the wavelength locking. The

423   discrepancy was traced to the fast fiber optic switches used to switch between the five OPO

424   wavelengths. The switches have a small amount of crosstalk and although the crosstalk was

425   initially measured to be relatively small, (~1-1.5%), the effect on the signal can be significant

426   especially at higher altitudes. Because of the crosstalk, the total signal received at each

427   wavelength has contributions from all five wavelengths. Wavelengths 1 and 5 (λ_1 and λ_5) are

428   "off line" and are not absorbed. Wavelengths 2, 3, 4 (λ_2, λ_3, λ_4) however, are absorbed and the

429   amount of absorption increases with altitude. As the altitude (absorption) increases the "on line"

430   wavelengths (λ_2, λ_3, λ_4) signals, have increasing contributions from the off line wavelengths (λ_1

431   and λ_5). Thus, a correction factor is needed to account for the crosstalk. The analysis of the

432   reference cell provided the initial evidence and estimate of the crosstalk correction factor.

433   Further refinement of the average correction factor at three different flight altitudes (3.1, 6.3 and

434   12.7 km) was obtained by ratioing the raw integrated pulse energies at wavelengths 1, 2, 4, and 5

435   to wavelength 3 and comparing the actual with the theoretical values. Obviously, the correction

436   factor values for different altitudes are just average estimates, not exact values and they vary

437   with altitude and topography. As the aircraft ascends or descends or the topography changes the

438   crosstalk factor will change. Furthermore, as the performance and gain of the OPO cavity

439   changes there is no guarantee that the crosstalk between wavelengths will remain fixed. The

440   crosstalk correction factor accounted for the observed discrepancy for the three constant flight

441   altitude segments of flight 3 (3.1, 6.3 and 12.7 km) and was applied to the analysis. Fig. 12

442   shows the time series data of the in-situ CH_4 mixing ratio from the Picarro, the theoretical CH_4

443   mixing ratio, set at 1900 ppb, and the retrieved CH_4 mixing ratio values for the three constant

444   flight altitude segments (3.1, 6.3 and 12.7 km) used in the analysis. When the outliers were

445 removed, the standard deviation of the retrieved CH$_4$ mixing ratio was 21.4 ppb or ~1.1 % (21.4

446 ppb/1900 ppb). The DOD Retrieval vs. DOD Theory linear fit (Fig. 13) had a slope of 1.01 and

447 an offset of -0.003. The R2 value was 0.999. These values are comparable but slightly worse to

448 those obtained during flight 1 and 2 with the OPA but the number of outliers that were filtered

449 out was higher.

450
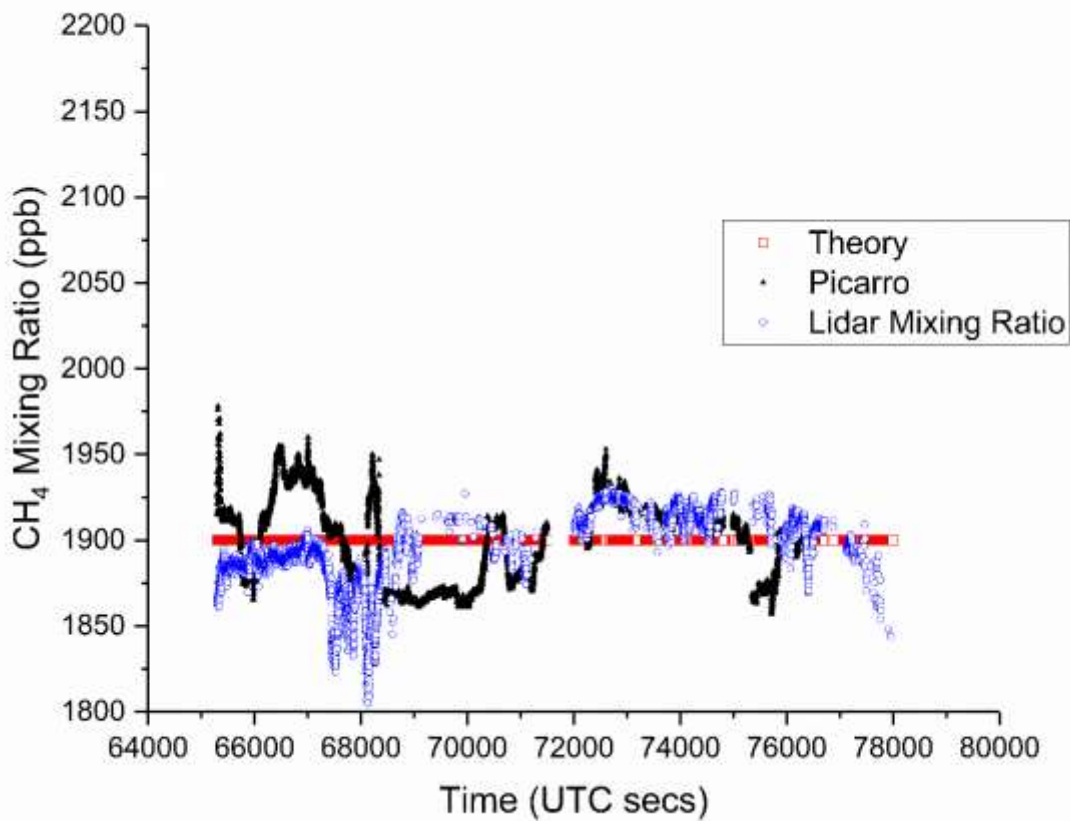

451
452 **Fig. 12** Time series for flight 3 data showing the in-situ CH$_4$ mixing ratio as measured by the Picarro, the theoretical
453 CH$_4$ mixing ratio (set at 1900 ppbv), and the CH$_4$ mixing ratio values by our retrieval algorithm.
454
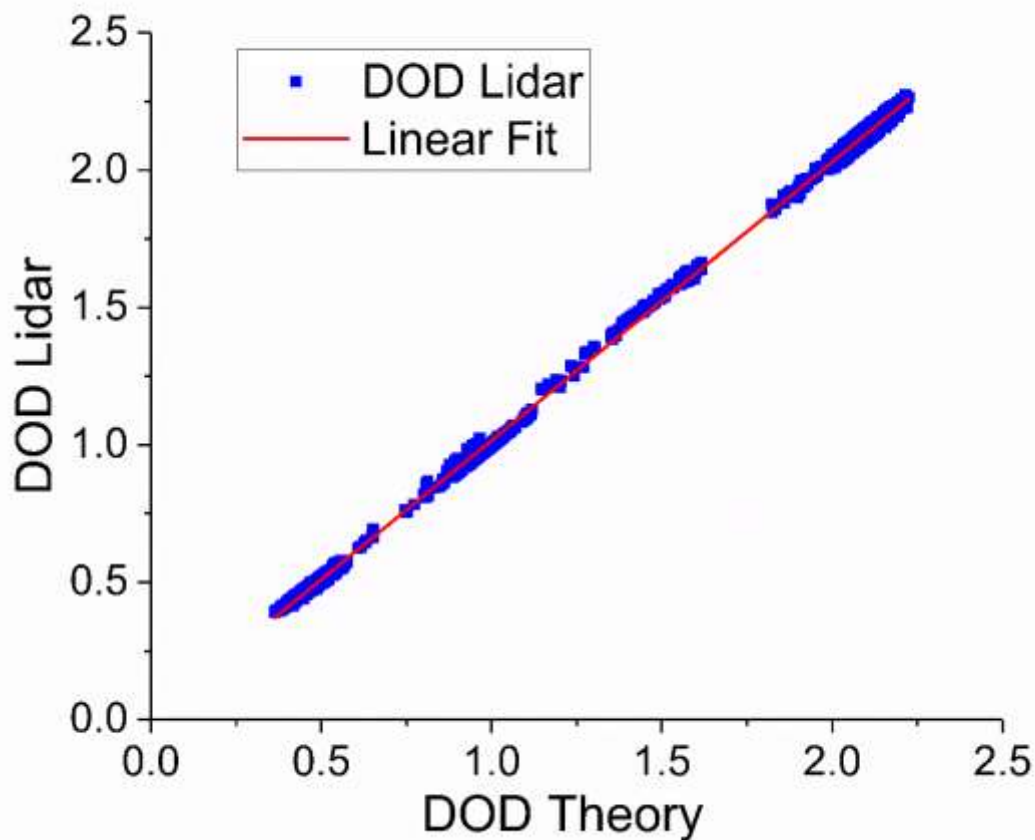
Fig. 13. Lidar DOD vs. Theoretical DOD for flight 3. The linear fit had a slope of 1.01 and an offset of -0.003. The R^2 value was 0.999.

4   Discussion

The high accuracy and precision needed for CH_4 measurements poses several challenges for the IPDA lidar design. Currently the laser transmitter poses the greatest challenge. The transmitter must have narrow linewidth (<100 MHz), must be tunable to scan over the CH_4 absorption line (~250 pm), and must have high pulse energy. The exact energy requirement also depends on the detector quantum efficiency, receiver aperture size, and other instrument parameters. Our link margin calculations show that approximately 600 μJ is needed for space to achieve a 0.5% random error with a 1 m diameter telescope.

467   We have tried to address several potential error sources in our instrument design: Errors due to

468   cloud and aerosol scattering are minimized by our pulsed approach, which digitizes the entire

469   atmospheric column return and gates the returns from the ground. The IPDA lidar cannot

470   penetrate optically thick clouds. However, our ranging algorithm provides accurate knowledge

471   of the total pathlength minimizing the effect of multiple scattering and excluding returns from

472   clouds. In order to improve the accuracy of the measurement better knowledge of the

473   spectroscopic parameters of the CH_4 line and a more sophisticated lineshape function are needed.

474   The CH_4 line we used is actually comprised of multiple lines with different linestrengths and

475   temperature dependence.

476   There are obvious difference between the instrument retrievals and those from the Picarro. The

477   lidar values show less variation in the CH_4 mixing ratio, which is to be expected since the Picarro

478   is an in-situ measurement and the lidar measures the column average. The Picarro recorded a

479   significant increase in the in-situ CH_4 mixing ratio only for flight 1 despite the fact that we tried

480   to target landfills and other areas of increased CH_4 mixing ratios. No significant CH_4 mixing

481   ratio increase was observed near these areas by the Picarro for flights 2 and 3. The biggest

482   increase was observed during the spiral for flight 1 near the ground (around 7000 secs UTC in

483   Fig. 8) when the lidar was turned off to satisfy the laser safety requirements. The other big

484   increase was observed earlier in the flight (around 6600-6700 secs UTC in Fig. 8). The source of

485   that increase is unclear.

486   The predicted values (i.e. "truth") to which our experimental data are fitted to, assumed a

487   constant CH_4 mixing ratio of 1900 ppb. The actual CH_4 mixing ratio profile over the entire flight

488   path is of course, unknown. Although 1900 ppb is clearly not an accurate estimate of the true

489   mixing ratio for an entire flight, it provided a reasonable basis for estimating the precision, but

490   not necessarily the absolute accuracy, of the IPDA lidar. In order to assess the accuracy of any

491   IPDA lidar multiple spirals and/or data from other sources such as radiosondes are needed to

492   measure the actual vertical distribution of CH_4 mixing ratio. Even then, differences and biases

493   will remain. Differences in the spectroscopic database (HITRAN 2012 vs. 2008), and effects

494   like line mixing and speed dependent profiles produce different results. Our incomplete

495   knowledge of the state of the atmosphere (pressure, temperature, and humidity) and the accuracy

496   of our meteorological model also contribute. Although the MERRA model was adequate for

497   these initial demonstration flights, in order to evaluate the IPDA lidar accuracy, better

498   knowledge and modeling of the state of the atmosphere and CH_4 vertical profiles at the local

499   level are needed. These can be obtained in future flights by increasing the frequency and

500   location of the spirals, including data from other instruments and radiosonde data if available.

501   Finally, lidar issues due to a variety of factors such as shot noise, ground reflectivity, speckle

502   noise, wavelength and power stability of the laser transmitter, etalon fringes, and in the case of

503   the OPO cross talk between wavelengths all contribute to biases in the measurement. With the

504   limited data obtained from these demonstration flights, we are not able to separate individual

505   bias sources. However, we did observe that the random noise was reduced by the expected

506   $1/\sqrt{t_{av}}$, where t_{av} is the averaging time, for up to ~5-10 secs. After ~5-10 secs, no improvement in

507   the noise statistics is observed.

508   The CH_4 IPDA lidar needs significant engineering improvements to increase its reliability. The

509   opto-mechanical design, laser transmitter stability, for both the OPA and OPO needs to be

510   considerably improved to reduce the effects of vibration, temperature and pressure. The locking

511   electronics and diagnostics for the seed lasers and OPO cavity also need to improve. The

512   isolation between OPO wavelengths needs to increase by at least an order of magnitude to

513   eliminate the need for crosstalk correction factors. All of these improvements are feasible if

514   proper engineering resources can be applied.

515   The OPA, which used 20 wavelengths, produced better fits, was simpler to implement than the

516   OPO because it did not require an optical resonator cavity, and was easier to align and tune.

517   However, it is extremely difficult to scale the OPA energy to that needed for space (~ 600 μJ

518   depending on the receiver size and other instrument parameters) and maintain a narrow

519   linewidth. The highest energy we obtained in the laboratory with our OPA was 290 μJ using a

520   two-stage OPA, and the burst-mode Yb fiber laser amplified by a custom solid-state amplifier as

521   a pump. However, at high energies, the OPA output spectrum typically consists of sharp peak

522   near the seed wavelength and a broad side lobe, when the parametric gain is high. In that case,

523   we cannot clearly define the linewidth but it is generally too wide for accurate CH_4 IPDA lidar

524   measurements. In addition, for a space mission we are aiming for a simple and efficient single

525   stage - not a complex multi-stage - OPA based on quasi-phase matching (QPM). In this

526   configuration, we have observed that the OPA output linewidth does not fully converge to the

527   seed linewidth, giving wide side lobes, especially when pump and seed fluences are high and

528   low, respectively[52]. Similar side lobes were observed in seeded QPM-based OPA system for a

529   CO_2 lidar[53]. Back-conversion and parametric amplification of the seed's side lobes are possible

530   causes. Complex OPA/OPG systems in other wavelength regions have been developed with a

531   narrow linewidth[54]. However, it is difficult to predict how they can be implemented with a

532   multi-wavelength IPDA lidar for space because of their complexity. If the seed laser power can

533   be significantly scaled up then it may be possible to achieve energies of 600 μJ out of the OPA

534   with a narrow linewidth. With the existing seed and pump laser technology, we do not see a path

535   to space for the OPA in the near future. However, it remains a viable transmitter for CH_4

536   measurements from an airborne platform.

537   In the OPO, narrow linewdith was achieved by using an optical resonator cavity, which also

538   enhances the energy of the non-linear conversion. Our 5-wavelength OPO uses a 1.2 mJ GSFC-

539   built solid-state pump laser and a triangular optical ring cavity. We have since replaced the

540   GSFC-built solid-state pump laser with a smaller, compact Yb fiber laser and redesigned the

541   OPO cavity to improve stability.   In the laboratory we demonstrated energies of ~250 μJ at 5

542   kHz with a narrow (transform limited) linewidth. The OPO energy could be scaled to space but

543   it requires complex optical phase-lock loops and cavity control.

544   In recent years, resonantly pumped Erbium (Er) doped YAG, Er:YAG and Er:YGG, lasers,

545   which directly emit at 1645.5 and 1650.96 nm, respectively offer another option for a CH_4

546   transmitter. Using Er:YAG for CH_4 detection dates back to 1972[55] and recent successful

547   demonstration and commercialization of high power and high spectral brightness pump sources

548   have afforded the realization of resonant pumping of Er:YAG[56-59] and Er:YGG[60, 61]. The

549   emission cross-section of Er:YAG crystal is centered near 1645.3 nm and falls off rapidly at

550   1650.96 nm. It is near the MERLIN lines at 1645.55 nm which are relatively wide (~56 pm).

551   Our CH_4 line at 1650.96 nm is narrower (~36 pm) which makes fast tuning easier. Unfortunately,

552   Er:YAG cannot be used as a gain medium at 1650.96 nm but Er:YGG can be used as a potential

553   medium for lasing at that wavelength. Both materials are good candidates for a CH_4 laser

554   transmitter. Power scaling for both materials, multi-wavelength operation and tuning

555   considerations remain.

556   Our preliminary radiative transfer calculations show that both lines (Er:YAG at 1645.55 nm and

557   Er:YGG at 1650.96 nm) have similar temperature sensitivity and are well suited for space born

558   CH$_4$ measurements. Recent high accuracy spectroscopic measurements indicate that line mixing

559   effects in the Er:YAG 1645.55 nm line[41] should also be taken into account. We expect similar

560   effects to be present for the Er:YGG line at 1650.96 nm.

561   **5   Summary**

562   We reported on an airborne demonstration of atmospheric CH$_4$ measurements with an Integrated

563   Path Differential Absorption (IPDA) lidar using an optical parametric oscillator (OPO) and

564   optical parametric amplifier (OPA) laser transmitter and sensitive avalanche photodiode detector.

565   The lidar measured the atmospheric CH$_4$ absorption at multiple, discrete wavelengths near

566   1650.96 nm. The instrument was deployed in 2015 aboard NASA's DC-8 airborne laboratory

567   and measured CH$_4$ mixing ratios from 2 km to 13 km. Relatively high precision measurements

568   of 0.7% to 1.1 % were demonstrated for all three flights however, many areas of improvement

569   remain. The stability and reliability of the laser transmitters need to improve considerably but the

570   basic measurement approach has been demonstrated. We are currently improving our airborne

571   instrument with better opto-mechanical design and compact, more stable laser transmitters. We

572   hope to fly again in the near future when the next opportunity arise.

589 **References**

590 1. Intergovernmental Panel on Climate Change, *IPCC Fifth Assessment Report,* Cambridge Univ.

591 Press, Cambridge, U. K. and New York. (2013).

592 2. Saunois, Marielle, Philippe Bousquet, Ben Poulter, Anna Peregon, Philippe Ciais, Josep G. Canadell,

593 Edward J. Dlugokencky et al. "The global methane budget 2000-2012." Earth System Science Data 8,

594 **no. 2,** 697**,** (2016).

595 3. Trends in Atmospheric Methane, https://www.esrl.noaa.gov/gmd/ccgg/trends_ch4/, accessed on May

596 4th 2017.

597 4. Fiore, A. M., D. J. Jacob, B. D. Field, D. G. Streets, S. D. Fernandes, and C. Jang, "Linking ozone

598 pollution and climate change: The case for controlling methane", Geophys. Res. Lett., **29** (19), 1919,

599 doi:10.1029/2002GL015601, 2002.

600 5. Franco, B., E. Mahieu, L. Emmons, Z. Tzompa-Sosa, E. Fischer, K. Sudo, B. Bovy, S. Conway, D.

601 Griffin, J. Hannigan, K. Strong, and K. Walker (2016), "Evaluating ethane and methane emissions

602 associated with the development of oil and natural gas extraction in North America", Environ. Res.

603 Lett., **11.**4 (2016).

604 6. Turner, A. J., D. J. Jacob, J. Benmergui, S. C. Wofsy, J. D. Maasakkers, A. Butz, O. Hasekamp, and

605 S. C. Biraud (2016), "A large increase in U.S. methane emissions over the past decade inferred from

606 satellite data and surface observations", Geophys. Res. Lett., 43, 2218–2224, (2016).

607 doi:10.1002/2016GL067987.

608 7. National Research Council Decadal Survey: *Earth Science and Applications from Space: National*

609 *Imperatives for the Next Decade and Beyond*, National Academic Press, 2007.

610 8. Schimel, David, et al. "Observing the carbon-climate system." *arXiv preprint arXiv:1604.02106*

611 (2016).

612   9. Dlugokencky, EJ; Steele, LP, Lang, PM, Masarie, K. A., "Atmospheric Methane at Mauna-Loa and

613   Barrow Observatories - Presentation and Analysis of In-Situ Measurements", J. Geophys. Res., **100**,

614   23103-23113, (1995).   DOI: 10.1029/95JD02460.

615 10. Prinn, R. G., et al. (2000), "A history of chemically and radiatively important gases in air deduced

616   from ALE/GAGE/AGAGE", J. Geophys. Res., **105** (D14), 17751– 17792, (2000).

617 11. Schuur, E.A.G., McGuire, A.D., Schädel, C., Grosse, G., Harden, J.W., Hayes, D.J., Hugelius, G.,

618   Koven, C.D., Kuhry, P., Lawrence, D.M. and Natali, S.M., "Climate change and the permafrost

619   carbon feedback". *Nature*, *520* (7546), pp.171-179, (2015).

620 12. Coheur, P.F., Xiong, X., C. D. Barnet, Q. Zhuang, T. Machida, C. Sweeney, and P. K. Patra, "Mid-

621   upper tropospheric methane in the high Northern Hemisphere: Spaceborne observations by AIRS,

622   aircraft measurements, and model simulations", J. Geophys. Res., **115**, D19309, (2010).

623   doi:10.1029/2009JD013796

624 13. Buchwitz, M., R. De Beek, J. P. Burrows, H. Bovensmann, T. Warneke, J. Notholt, J. F. Meirink, A.

625   P. H. Goede, P. Bergamaschi, S. Körner, M. Heimann, A. Schulz, "Atmospheric methane and carbon

626   dioxide from SCIAMACHY satellite data: initial comparison with chemistry and transport models",

627   Atmos. Chem. Phys., 5, 941–962, (2005).

628 14. Bergamaschi, P., Frankenberg, C., Meirink, J.F., Krol, M.C., Dentener, F.J.; Wagner, T., Platt, U.,

629   Kaplan, J.O., Körner, S.; Heimann, M.; Dlugokencky, E.J.; Goede, A. De, "Satellite chartography of

630   atmospheric methane from SCIAMACHY on board ENVISAT: 2. Evaluation based on inverse model

631   simulations", Journal of Geophysical Research-Atmospheres, Volume: **112**, pp. D02304/1-

632   D02304/26, (2007).

633 15. Wecht, K. J., Jacob, D. J., Wofsy, S. C., Kort, E. A., Worden, J. R., Kulawik, S. S., Henze, D. K.,

634   Kopacz, M., and Payne, V. H., "Validation of TES methane with HIPPO aircraft observations:

635   implications for inverse modeling of methane sources", Atmos. Chem. Phys., **12**, 1823-1832,

636   doi:10.5194/acp-12-1823-2012, (2012).

637   16. August, T., Klaes, D., Schlussel, P., Hultberg, T., Crapeau, M., Arriaga, A., O'Carroll, A., Coppens,

638   D., Munro, R., Calbet, X., "IASI onMetop-A: Operational Level 2 retrievals after five years in orbit",

639   Journal of Quantitative Spectroscopy & Radiative Transfer **113**, 1340–1371, (2012).

640   17. Yokota, T., Y. Yoshida, N. Eguchi, Y. Ota, T. Tanaka, H. Watanabe, and S. Maksyutov, "Global

641   Concentrations of CO2 and CH4 Retrieved from GOSAT: First Preliminary Results", SOLA, Vol. **5**,

642   160–163, (2009). doi:10.2151/sola.2009–041

643   18. Zona, Donatella, Beniamino Gioli, Róisín Commane, Jakob Lindaas, Steven C. Wofsy, Charles E.

644   Miller, Steven J. Dinardo et al. "Cold season emissions dominate the Arctic tundra methane budget."

645   *Proceedings of the National Academy of Sciences* **113**, no. 1, 40-45, (2016).

646   19. Stephan, C., M. Alpers; B. Millet; G. Ehret; P. Flamant; C. Deniel, "MERLIN: a space-based

647   methane monitor", "Lidar Remote Sensing for Environmental Monitoring XII. Proceedings of the

648   SPIE, Volume 8159, pp. 815908-815908-15, (2011).

649   20. Kiemle, M. Quatrevalet, G. Ehret, A. Amediek, A. Fix, and M. Wirth, "Sensitivity studies for a space-

650   based methane lidar mission", Atmos. Meas. Tech. Discuss., 4, 3545–3592, 2011.

651   21. Measures, R., *Laser Remote Sensing,* Chapter 7, John Wiley & Sons, New York, 1984

652   22. Abshire, J.B., H. Riris, C. Weaver, J. Mao, G. Allan, W. Hasselbrack, and E. Browell, "Airborne

653   measurements of CO2 column absorption and range using a pulsed direct-detection integrated path

654   differential absorption lidar," Appl. Opt. 52, 4446-4461 (2013).

655   23. Ehret, G., Kiemel, C., Wirth W., Amediek, A., et.al, "Space-borne remote sensing of CO_2, CH_4, and

656   N2O by integrated path differential absorption lidar: a sensitivity analysis", Appl. Phys. B 90, 593-

657   608, (2008).

658   24. A. Amediek, Fix, A., Wirth, M., Ehret, G., "Development of an OPO system at 1.57 μm for integrated

659   path DIAL measurement of atmospheric carbon dioxide", Appl. Phys. B **92**, 295–302, DOI:

660   10.1007/s00340-008-3075-6, (2008).

661   25. Riris, H., K. Numata, S. Li, S. Wu, A. Ramanathan, M. Dawsey, J. Mao, R. Kawa, and J. Abshire,

662   "Airborne measurements of atmospheric methane column abundance using a pulsed integrated-path

663   differential absorption lidar," Appl. Opt. **51**, 8296-8305 (2012).

664   26. Riris, H., M. Rodriguez, G.R. Allan, W. Hasselbrack, J. Mao, M. Stephen, J. Abshire, "Pulsed

665   airborne lidar measurements of atmospheric optical depth using the Oxygen A-band at 765 nm,"

666   Applied Optics, **52**(25), 6369-6382 (2013).

667   27. Spiers, Gary D., et al. "Atmospheric CO 2 measurements with a 2 μm airborne laser absorption

668   spectrometer employing coherent detection." Applied Optics **50**.14, 2098-2111, (2011).

669   28. Dobler, Jeremy T., et al. "Atmospheric CO_2 column measurements with an airborne intensity-

670   modulated continuous wave 1.57 μm fiber laser lidar." Applied Optics **52**.12, 2874-2892, (2013).

671   29. Amediek, A., G. Ehret, A. Fix, M. Wirth, C. Büdenbender, M. Quatrevalet, C. Kiemle, and

672   C. Gerbig, "CHARM-F-a new airborne integrated-path differential-absorption lidar for

673   carbon dioxide and methane observations: measurement performance and quantification of

674   strong point source emissions," Appl. Opt. **56**, 5182-5197 (2017).

675   30. Fix, Andreas, Axel Amediek, Christian Büdenbender, Gerhard Ehret, Mathieu Quatrevalet,

676   Martin Wirth, Jens Löhring et al., "Development and first results of a new near-ir airborne

677   greenhouse gas lidar", Optics and Photonics for Energy and the Environment, pp. EM3A-3,

678   Optical Society of America, (2015).

679   31. Amediek, Axel, Gerhard Ehret, Andreas Fix, Martin Wirth, M. Quatrevalet, C. Büdenbender,

680   C. Kiemle, J. Loehring, and C. Gerbig. "First airborne IPDA lidar measurements of methane

681   and carbon dioxide applying the DLR greenhouse gas sounder CHARM-F", AGU Fall

682   Meeting Abstracts, (2015).

683   32. Rothman, L. S., et al. "The HITRAN 2008 molecular spectroscopic database." Journal of Quantitative

684   Spectroscopy and Radiative Transfer, **110,** 9, 533-572, (2009).

685   33. Chen, Jeffrey R., Kenji Numata, and Stewart T. Wu. "Error reduction in retrievals of atmospheric

686   species from symmetrically measured lidar sounding absorption spectra." Optics express **22**.21,

687   26055-26075, (2014).

688   34. Ramanathan, A., Jianping Mao, Graham R. Allan, Haris Riris, Clark J. Weaver, William E.

689   Hasselbrack, Edward V. Browell, James B. Abshire, "Spectroscopic measurements of a CO_2

690   absorption line in an open vertical path using an airborne lidar," Applied Physics Letters, **103**, 214102

691   (2013), DOI:http://dx.doi.org/10.1063/1.4832616

692   35. Allan, G. R., H. Riris, W. Hasselbrack, M. Rodriguez, A. Ramanathan, X. Sun, J. Mao, and J. B.

693   Abshire. "Atmospheric Backscatter Profiles at 765nm and 1572nm from Pulsed Lidar Measurements

694   of CO2 and O2 Column Absorption from the 2013 ASCENDS Flight Campaign." AGU Fall Meeting

695   Abstracts, **vol. 1**, p. 0211, (2013).

696   36. Ramanathan, Anand K., Jianping Mao, James B. Abshire, and Graham R. Allan. "Remote sensing

697   measurements of the CO2 mixing ratio in the planetary boundary layer using cloud slicing with

698   airborne lidar." *Geophysical Research Letters* **42**, no. 6, 2055-2062, (2015).

699   37. Numata, K., Riris, H., S. Li, S. Wu, S. R. Kawa, M. Krainak, J. Abshire, "Ground demonstration of

700   trace gas lidar based on optical parametric amplifier", Journal of Applied Remote Sensing, **Vol. 6**,

701   063561-1, (2012).

702   38. Engin, Doruk, Ibraheem Darab, John Burton, Jean-Luc Fouron, Frank Kimpel, Brian Mathason,

703   Shantanu Gupta, and Mark Storm. "Highly-efficient, high-energy pulse-burst Yb-doped fiber laser

704   with transform limited linewidth." In *SPIE Defense+ Security*, pp. 908112-908112. International

705   Society for Optics and Photonics, (2014).

706   39. Numata, K., Riris, H., Wu, S., "Fast-switching methane lidar transmitter based on a seeded optical

707   parametric oscillator", Applied Physics B, **116**, 4, 959-966, (2014).

708   40. Numata, Kenji, Jeffrey R. Chen, and Stewart T. Wu. "Precision and fast wavelength tuning of a

709   dynamically phase-locked widely-tunable laser." Optics express **20.13**, 14234-14243, (2012).

710   41. Drever, R.W.P., J.L. Hall, F.V. Kowalski, J. Hough, G.M. Ford, A.J. Munley, H. Ward, Appl. Phys.

711   B, **31**, 97–105, (1983).

712   42. Fix, Andreas, Renaud Matthey, Axel Amediek, Gerhard Ehret, Florian Gruet, Christoph Kiemle,

713   Volker Klein, Gaetano Mileti, Joao Pereira do Carmo, and Mathieu Quatrevalet, "Investigations on

714   frequency and energy references for a space-borne integrated path differential absorption lidar",

715   Proceedings of the International Conference on Space Optics, **vol. 10**, (2014).

716   43. Beck, Jeff, et al. "A highly sensitive multi-element HgCdTe e-APD detector for IPDA lidar

717   applications." *Journal of Electronic Materials* **43**.8, 2970-2977, (2014).

718   44. Sun, Xiaoli, James B. Abshire, and Jeffrey D. Beck. "HgCdTe e-APD detector arrays with

719   single photon sensitivity for space lidar applications." SPIE Sensing Technology+

720   Applications. International Society for Optics and Photonics, (2014).

721   45. Sun, Xiaoli, James B. Abshire, Jeffrey D. Beck, Pradip Mitra, Kirk Reiff, and Guangning

722   Yang. "HgCdTe avalanche photodiode detectors for airborne and spaceborne lidar at infrared

723   wavelengths." Optics Express 25, **14**, 16589-16602, (2017).

724   46. Abshire, J.B., Ramanathan, A.; Riris, H.; Mao, J.; Allan, G.R.; Hasselbrack, W.E.; Weaver, C.J.;

725   Browell, E.V. "Airborne Measurements of CO2 Column Concentration and Range Using a Pulsed

726   Direct-Detection IPDA Lidar," Remote Sensing 2014, 6, 443-469, (2014)

727   47. Amediek, A., X. Sun, and J. B. Abshire, "Analysis of Range Measurements from a Pulsed Airborne

728   CO2 Integrated Path Differential Absorption Lidar", Transactions on Geoscience and Remote

729   Sensing, **51**, No. 5, (2013).

730   48. Clough, S.A. and M.J. Iacono, M,I., "Line-by-line calculations of atmospheric fluxes and

731   cooling rates. 2: Applications to carbon dioxide, ozone, methane, nitrous oxide, and the

732   halocarbons," J. of Geophys. Res. **100**,16519-16535, (1995).

733   49. Delahaye, T., S. E. Maxwell, Z. D. Reed, H. Lin, J. T. Hodges, K. Sung, V. M. Devi, T. Warneke, P.

734   Spietz, and H. Tran, "Precise methane absorption measurements in the 1.64 μm spectral region for the

735   MERLIN mission." Journal of Geophysical Research: Atmosphere*s* **121**.12, 7360-7370, (2016).

736   50. Bosilovich, Michael G., "Regional Climate and Variability of NASA MERRA and Recent

737   Reanalyses: U.S. Summertime Precipitation and Temperature", J. Appl. Meteor.

738   Climatology, **52**, 1939–1951, (2013). doi: http://dx.doi.org/10.1175/JAMC-D-12-0291.

739   51. Rienecker, M.M., Suarez, M.J., Gelaro, R.; Todling, R., Bacmeister, J., Liu, E.; Bosilovich,

740   M.G., Shubert, S.D., Takacs, L., Kim, G.-K., et al., "MERRA: NASA's modern-era

741   retrospective analysis for research and applications". J. of Climate, **24**, 3624–3648, (2011).

742   52. Li, Steven, Haris Riris, Kenji Numata, Stewart Wu, Demetrios Poulios, Anand Ramanathan,

743   James Abshire, and Michael Krainak. "Tunable narrow linewidth laser source for a methane

744   lidar," Aerospace Conference, 2012 IEEE, pp. 1-8. IEEE, (2012).

745   53. Shibata, Yasukuni, Chikao Nagasawa, and Makoto Abo. "Development of 1.6 μm DIAL

746   using an OPG/OPA transmitter for measuring atmospheric CO2 concentration profiles."

747   Applied Optics 56, **no. 4**, 1194-1201, (2017).

748   54. Kulatilaka, W. D., et al. "Development of injection-seeded, pulsed optical parametric

749   generator/oscillator systems for high-resolution spectroscopy," Applied Physics B: Lasers

750   and Optics, **80.6**, 669-680, (2005).

751   55. White, Kenneth O., and Stuart A. Schleusener. "Coincidence of Er: YAG laser emission with

752   methane absorption at 1645.1 nm." Applied Physics Letters **21**.9, 419-420, (1972).

753   56. Wang, X., et al. "Dual-wavelength Q-switched Er: YAG laser around 1.6 μm for methane

754   differential absorption lidar." *Laser Physics Letters* 10.11 (2013): 115804.

755   57. Tang, Pinghua, et al. "Stable and wavelength-locked Q-switched narrow-linewidth Er: YAG

756   laser at 1645 nm." Optics express **23**.9, 11037-11042, (2015).

757   58. Fritsche, H., O. Lux, X. Wang, Z. Zhao, and H. J. Eichler. "Resonantly diode pumped Er:

758   YAG laser systems emitting at 1645 nm for methane detection." Laser Physics Letters **10**, no.

759   10, 105805, (2013).

760   59. Gao, Chunqing, Lingni Zhu, Ran Wang, Mingwei Gao, Yan Zheng, and Lei Wang. "6.1 W

761   single frequency laser output at 1645 nm from a resonantly pumped Er: YAG nonplanar ring

762   oscillator." *Optics letters* 37, no. **11**, 1859-1861, (2012).

763   60. Kudryashov, Igor, and Evgenii Kotelnikov. "Tunable Q-switched Solid State Laser for

764   Methane Detection." SPIE LASE, pp. 100821I-100821I, International Society for Optics and

765   Photonics, 2017.

766   61. M Mackenzie, Jacob, James Grant-Jacob, Stephen Beecher, Haris Riris, Anthony Yu, David

767   Shepherd, and Robert Eason, "Er:YGG planar waveguides grown by pulsed laser deposition

768   for LIDAR applications." SPIE LASE, 100820A-100820A, International Society for Optics

769   and Photonics, 2017.

770

771   Figure Captions

772

773   Fig. 1. Two-way atmospheric transmittance near 1650.96 nm a from a 400 km orbit using the
774   2008 HITRAN database and a US standard atmosphere. The CH_4 line is mostly isolated
775   from adjacent CO_2 and H_2O vapor lines.
776   Fig. 2. Simplified functional block diagram of our IPDA lidar. The lidar can use one of two
777   different laser transmitters using a movable selection mirror: An Optical Parametric
778   Amplifier (OPA) or an Optical Parametric Oscillator (OPO). The transmitters use DFB
779   diode lasers for seed lasers but different pump lasers. Only one laser transmitter is operating
780   during flight.
781   Fig. 3. Example of temporal shape of the OPA burst pulse from the energy monitor detector
782   showing individual pulses within the burst pulse.
783   Fig. 4. The GSFC IPDA lidar installed on the NASA DC-8 airborne laboratory, in Palmdale,
784   CA. The transceiver structure supported two optical benches for the OPO and OPA, the
785   receiver telescope, and the transmit optics components. The overall transceiver dimensions
786   were approximately $0.9 \times 2.0 \times 0.8$ m3 and the total weight was 363 kg. Two instruments racks
787   on either side of the transceiver contained the control and data acquisition electronics.
788   Fig. 5 Fight tracks for the 2015 flights. Flight 1 (blue), Flight 2 (red), Flight 3 (magenta).
789   Fig. 6. Flight altitude (range) in m vs. time in UTC seconds since midnight as measured by
790   the GPS receiver and our IPDA lidar for all three flights. The differences between the GPS
791   and the IPDA lidar range are due to topography. The GPS measures the altitude above the
792   mean sea level (or reference ellipsoid) but the IPDA lidar range is the altitude (range) above
793   ground, which includes the topography.
794   Fig. 7 Theoretical CH_4 transmittance from a 400 km altitude with a US standard atmosphere
795   and a comparison of the approximate wavelength sampling by the OPA (black open squares,
796   20 wavelengths) and OPO (red solid circles, 5 wavelengths). For clarity, the OPO
797   wavelengths are labeled $\lambda_1, \lambda_2, \lambda_3, \lambda_4, \lambda_5$).
798   Fig. 8. Time series data for flight 1 showing the in-situ CH_4 mixing ratio as measured by the
799   Picarro, the theoretical CH_4 mixing ratio (set at 1900 ppbv), and the CH_4 mixing ratio values
800   by our retrieval algorithm. Outliers due to instrument adjustments and clouds were filtered
801   out.
802   Fig. 9. Lidar DOD vs. Theoretical DOD for flight 1. The linear fit (without the outliers) had a
803   slope of 0.98 and an offset of -0.007 and R^2 value was 0.994.
804   Fig. 10 Time series for flight 2 data showing the in-situ CH_4 mixing ratio as measured by the
805   Picarro, the theoretical CH_4 mixing ratio (set at 1900 ppbv), and the CH_4 mixing ratio values
806   by our retrieval algorithm. Outliers due to instrument adjustments and clouds were filtered
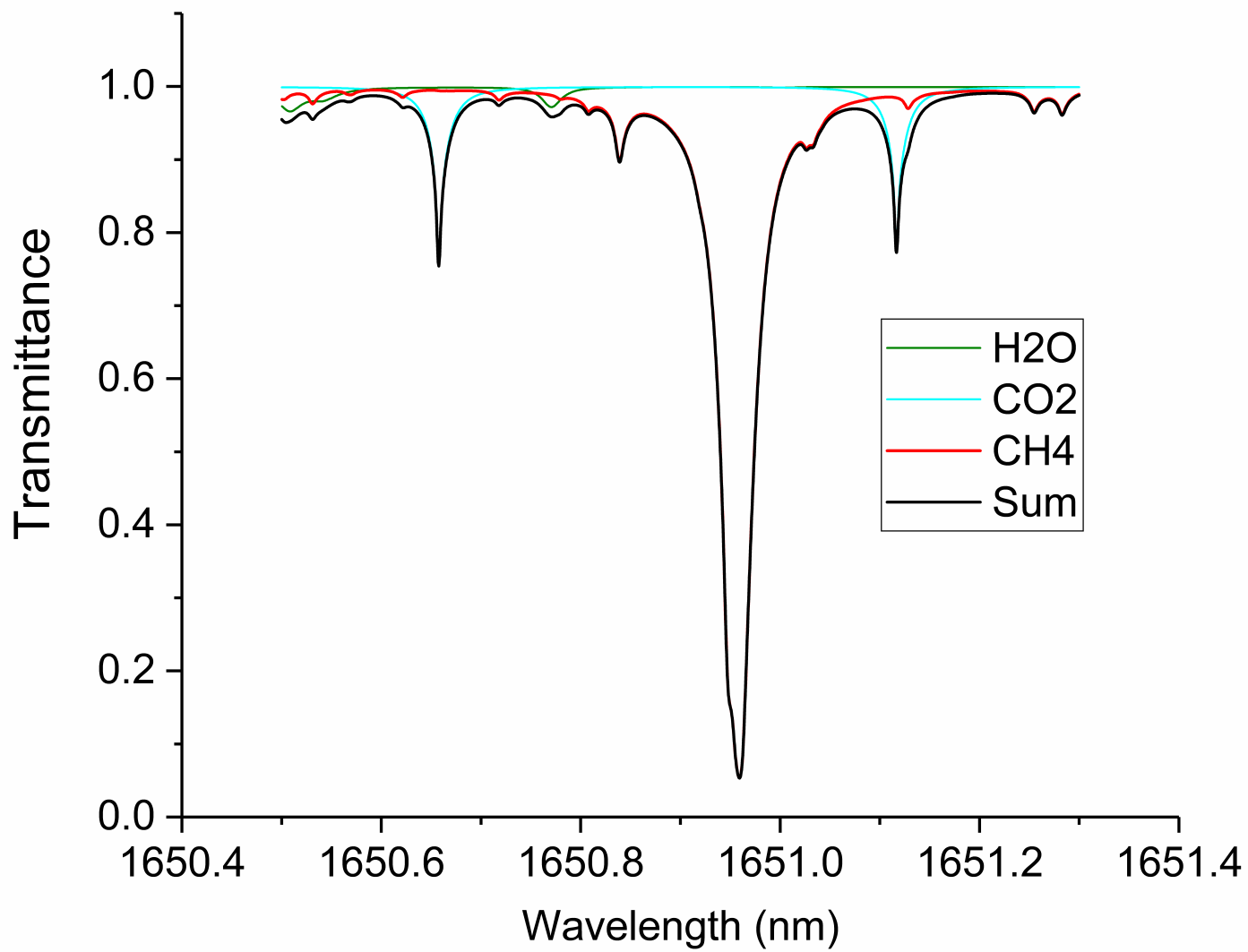807   out.
808   Fig. 11. Lidar DOD vs. Theoretical DOD for flight 2. The linear fit (without the outliers) had
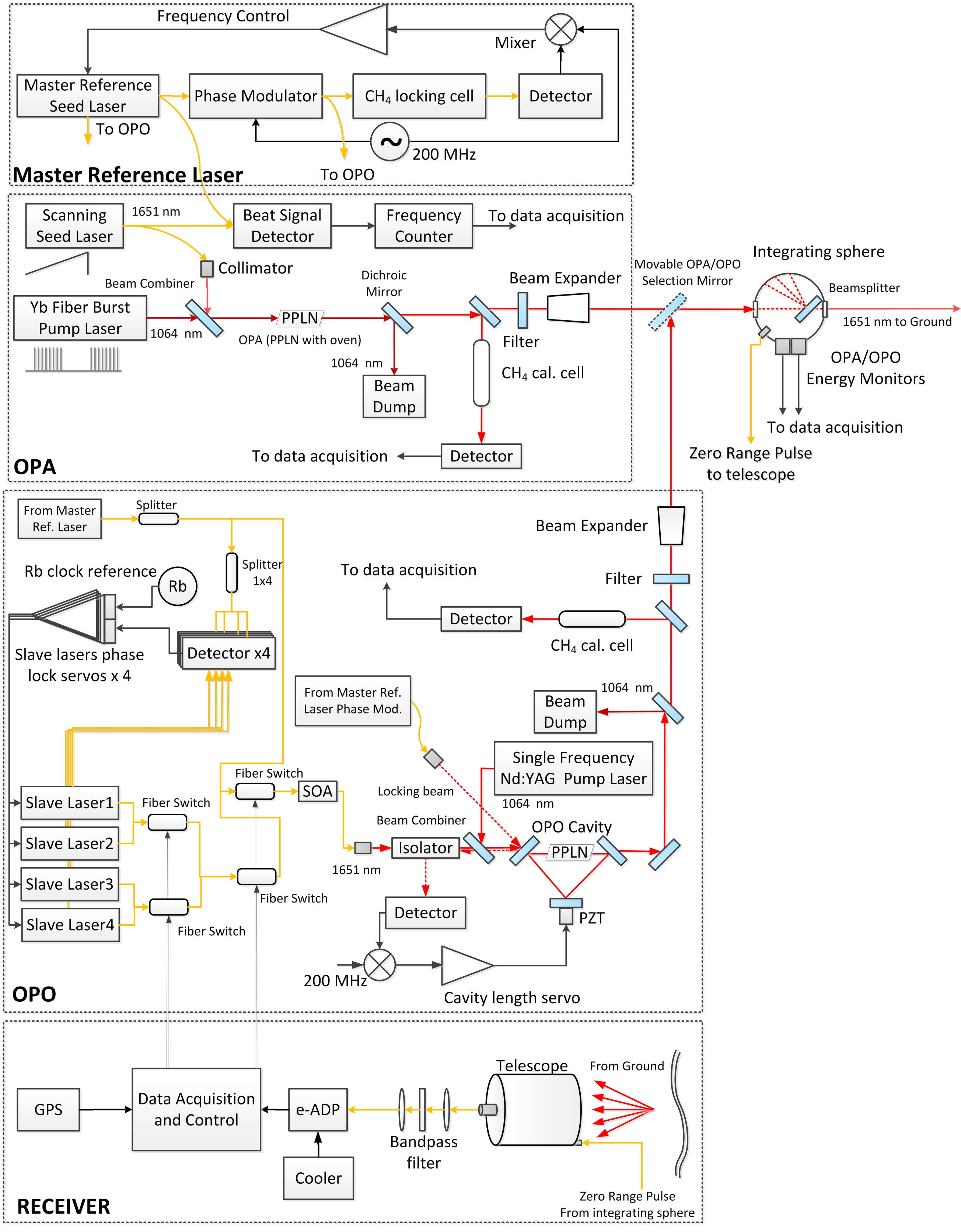809   a slope of 0.998 and an offset of -0.007 and R^2 value was 0.990.
810   Fig. 12 Time series for flight 3 data showing the in-situ CH_4 mixing ratio as measured by the
811   Picarro, the theoretical CH_4 mixing ratio (set at 1900 ppbv), and the CH_4 mixing ratio values
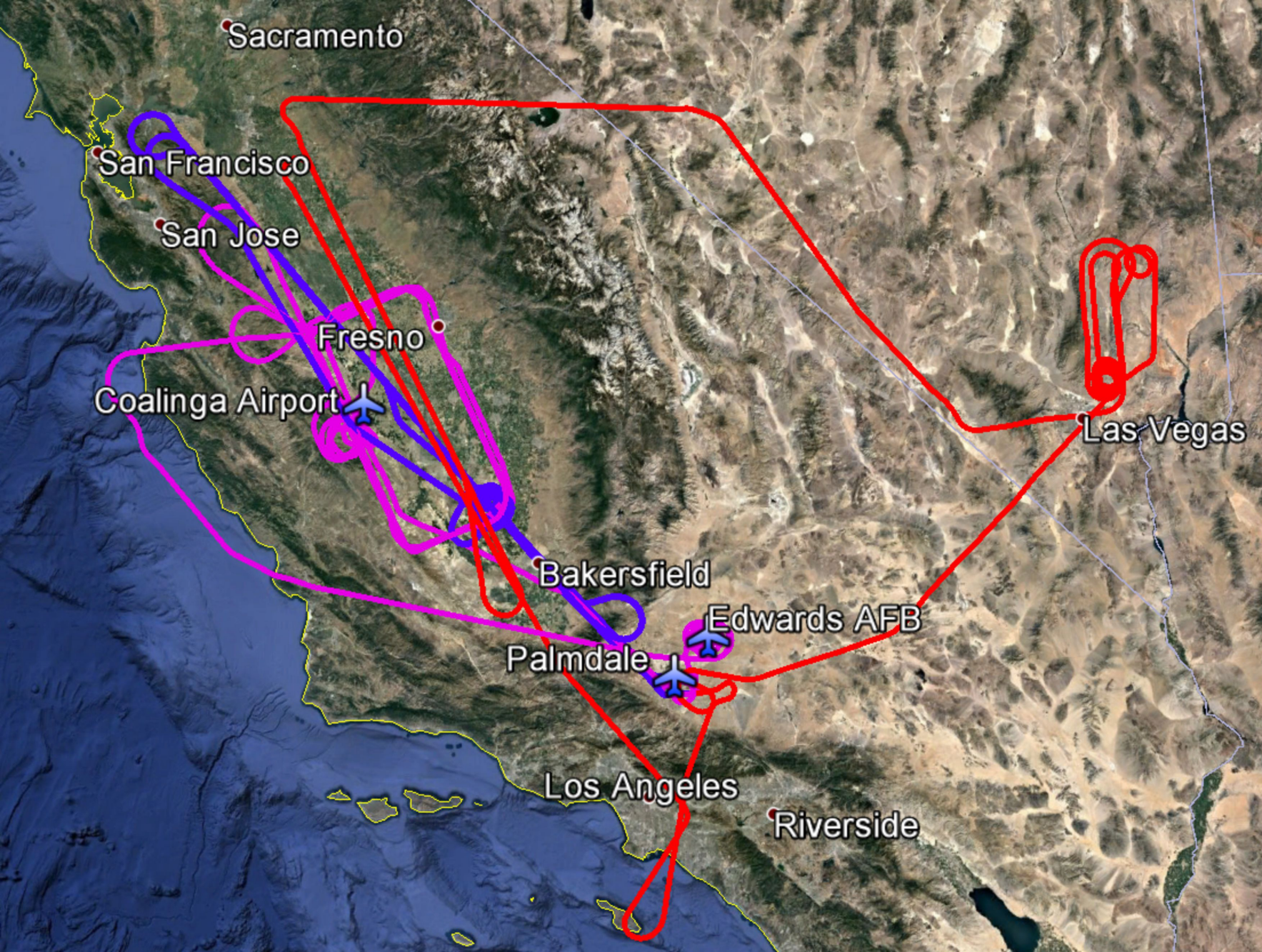812   by our retrieval algorithm.
813   Fig. 13. Lidar DOD vs. Theoretical DOD for flight 3. The linear fit had a slope of 1.01 and
814   an offset of -0.003. The R^2 value was 0.999.

Frequency Control

Mixer

Master Reference
Seed Laser

To OPO

Phase Modulator

CH$_4$ locking cell

Detector

200 MHz

To OPO

Master Reference Laser

Scanning
Seed Laser

1651 nm

Beat Signal
Detector

Frequency
Counter

To data acquisition

Collimator

Beam Combiner

Dichroic
Mirror

Beam Expander

Movable OPA/OPO
Selection Mirror

Integrating sphere

Beamsplitter

Yb Fiber Burst
Pump Laser

1064 nm

PPLN

OPA (PPLN with oven)

1064 nm

Beam
Dump

Filter

CH$_4$ cal. cell

1651 nm to Ground

OPA/OPO
Energy Monitors

To data acquisition

Zero Range Pulse
to telescope

To data acquisition

Detector

OPA

From Master
Ref. Laser

Splitter

Beam Expander

Rb clock reference

Rb

Splitter
1x4

Filter

To data acquisition

Detector

CH$_4$ cal. cell

Slave lasers phase
lock servos x 4

Detector x4

From Master Ref.
Laser Phase Mod.

1064 nm

Beam
Dump

Fiber Switch

SOA

Locking beam

Single Frequency
Nd:YAG Pump Laser

1064 nm

Slave Laser1

Fiber Switch

Fiber Switch

Beam Combiner

OPO Cavity

Slave Laser2

1651 nm

Isolator

PPLN

Slave Laser3

Fiber Switch

Slave Laser4

Fiber Switch

Detector

PZT

200 MHz

Cavity length servo

OPO

GPS

Data Acquisition
and Control

e-ADP

Telescope

From Ground

Bandpass
filter

Cooler

Zero Range Pulse
From integrating sphere

RECEIVER